11-4-2011

A Novel approach to engineering structures of a solid oxide fuel cell (SOFC): 3D direct write technology

Prasanna Khatri-Chhetri

ROCHESTER INSTITUTE OF TECHNOLOGY

A Novel Approach to Engineering Structures of a Solid Oxide Fuel Cell (SOFC): 3D Direct Write Technology

A Thesis submitted in partial fulfillment of the

requirements for the degree of

Master of Science in Industrial Engineering

in the

Department of Industrial & Systems Engineering

Kate Gleason College of Engineering

by

Prasanna Khatri-Chhetri

M.S., Industrial Engineering, Rochester Institute of Technology, 2011.

KATE GLEASON COLLEGE OF ENGINEERING

ROCHESTER INSTITUTE OF TECHNOLOGY

ROCHESTER, NEW YORK

CERTIFICATE OF APPROVAL

11/4/2011

M.S. DEGREE THESIS

The M.S. Degree Thesis of Prasanna Khatri-Chhetri

has been examined and approved by the

thesis committee as satisfactory for the

thesis requirement for the

Master of Science degree.

Approved by:

_____

Dr. Denis Cormier, Thesis Advisor

_____

Dr. Marcos Esterman, Committee Member

ABSTRACT

This thesis centers on the use of 3D direct write printing processes to produce Solid Oxide Fuel Cell (SOFC) structures having engineered porosity and macro structure. The objective of the work presented here is to be able to locally control porosity in the anode and cathode structure using 3D direct write printing methods. It is well understood that grading the electrodes enhances the SOFC's performance. A hierarchically graded porous electrode structure, varying from smallest pores at the electrode/electrolyte interface to largest pores at electrode/gas interface can be printed via 3D direct write methods. Layers as thin as 15µm have been achieved using this process. The change in the degree of electrode porosity achieved by varying the graphite loading fraction has been experimentally mapped out. The feasibility of changing the composition/porosity within a layer has been demonstrated, which also opens up possibilities for varying chemical composition within a layer/plane.

The second contribution of this work centers on the synthesis of a channeled electrode architecture aimed at producing structures with extremely low tortuosity. The proposed direct-write synthesis approach overcomes limitations of alternative approaches by allowing symmetric ribs and channels to be printed that balance out shrinkage stresses. The proposed channel architecture has been demonstrated, and models correlating process parameters with resulting surface area have been developed.

ACKNOWLEDGEMENT

First and foremost, I have to thank my family for their love and continuous support of my education.

I would like to acknowledge my advisor, Dr. Denis Cormier, for his guidance and support throughout this study. I would like to thank colleagues Sundaresan Balasubramanian and Anuj Datar for their efforts. I would also like to thank Qiang Liu from University of South Carolina, Columbia, SC for carrying out the tests.

The work is supported by Heterogeneous Functional Materials Center (HeteroFoam), an Energy Frontier Research Center (ERFC) funded by the U.S. Department of Energy and Office of Basic Energy Sciences under Award Number DE-SC0001061.

TABLE OF CONTENTS

TABLE OF FIGURES

LIST OF TABLES

CHAPTER 1: INTRODUCTION

1.1 POROUS MATERIALS

Porous materials are solids containing pores or voids. Porosity is defined as the fraction of the pore volume to the total volume occupied by the structure. Porous materials typically have a porosity range of 0.2-0.95 (2% - 95%). According to "The International Union of Pure and Applied Chemistry (IUPAC)", porous material can be classified based on their pore sizes as a) Macroporous (50nm<pore diameter), b) Mesoporous (2nm < pore diameter < 50nm) or c) Microporous (pore diameter < 2nm) [1]. The mechanical properties of porous materials are heavily influenced by pore size, pore geometry and the magnitude of porosity.

Porous metals, ceramics and glasses are already in use in various industrial applications involving chemistry, biotechnology, mechanical design and electronics. These porous materials have various applications from daily necessities (e.g. purifying water with porous ceramic filters), to use in modern industries (e.g. removal of dust from high purity process gases for semiconductor production). Depending on the application, different pore sizes, shapes, local distributions and pore orientations are required [1]. For instance, porosity and pore size in biomaterial scaffolds play a critical role in bone formation and in-growth in vitro and in vivo. For in vitro testing, lower porosities have been shown to be more effective, whereas higher porosities and pore sizes have been shown to be more effective for in vivo testing. However, mechanical properties diminish with increasing porosity, thereby setting a limit for pore size and porosity. Thus, a balance must be reached depending on mechanical loading to be experienced with the scaffold [2].

The research presented here focuses on engineering the geometric structure of porous electrodes (anode and cathode) of a Solid Oxide Fuel Cell (SOFC) using 3D Direct Write

Technology (DW printing). The objective is to locally control the size and shape of pores in the anode and cathode layers. The geometric structure, in turn, defines the pore morphology and how porous the structure is. Porous materials play a vital role in the development of fuel cell technology. The functions of these materials include the mass transport of gases to and from the active sites, the mechanical support of the fuel cell structure, and the conduction of electrons and ions [3]. The porous electrode properties significantly affect cell performance through their influence on electrochemical properties such as activation energy, ohmic resistance, exchange current density, etc [4]. Furthermore, graded porous anode structures of a SOFC can be designed to optimize the gas transport through the substrate in order to maintain high electrochemical activity for fuel oxidation at the anode/ electrolyte interface [5].

1.2 SOLID OXIDE FUEL CELLS (SOFC)

SOFC's are electrochemical devices that convert chemical energy directly into electrical energy without the need for combustion. The advantages of SOFC's include high efficiencies, fuel adaptability, low emissions, low noise and reliability. One major advantage SOFC's over other fuel cell technologies is the fuel adaptability. Most fuel cell technologies operate with pure hydrogen, whereas SOFC's can be made to run on a variety of fuels, such as hydrogen, methane, butane, natural gas, diesel, gasoline, etc. SOFC components are typically composed of ceramic materials and consist of no moving parts. Due to the use of ceramic materials, the cells can operate at temperatures as high as 1,000°C. This produces exhaust gases at temperatures ideal for use in combined heat and power applications and combined-cycle electric power plants. SOFC's can be manufactured using many of the techniques employed today in the electronics industry [6][7].

The components of a SOFC include an anode, electrolyte, cathode and interconnects. A SOFC cell consists of two porous electrodes separated by a solid gas tight electrolyte (Figure 1). During operation, fuel is introduced to the anode, and oxygen is introduced to the cathode. Oxygen (O_2) molecules are reduced at the cathode and are transported through the electrolyte layer to the anode. Oxidation of the ions then takes place in the anode, thus creating electrons and water. When a load is connected, the liberated electrons travel from the anode through the external load device and then back to the cathode (Figure 1). The current created by one cell is very small, so SOFC's are typically connected in series for a stack that meet the needs of the application. The power created from a SOFC depends on the rate at which the fuel disassociates to create electrons in the anode and the rate at which oxygen ions combine with hydrogen to form water. An interconnect layer separates each individual cell.

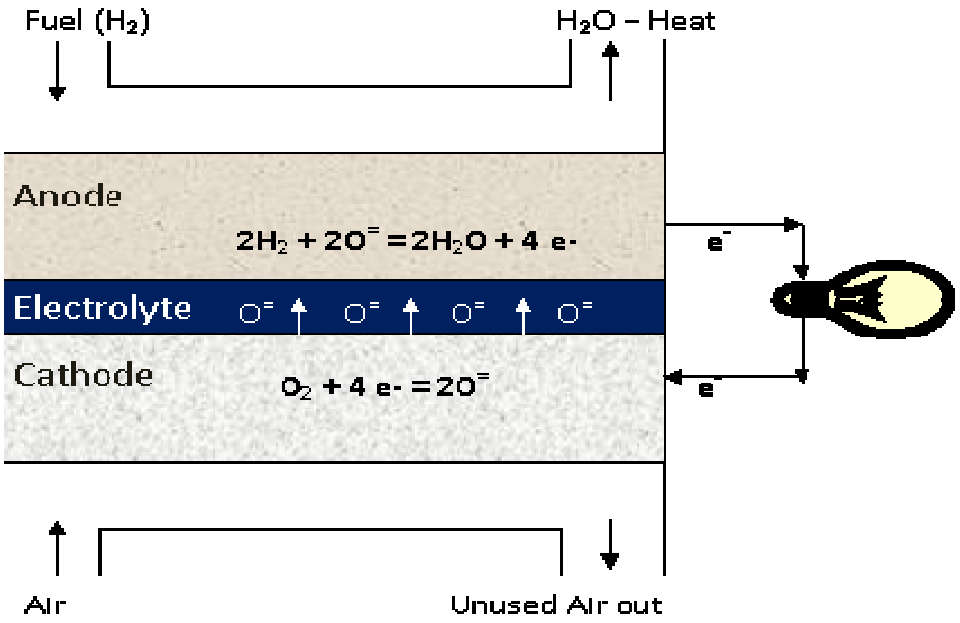

Figure 1 Solid Oxide Fuel Cell (Not to scale)

Each SOFC component has specific material characteristics and porosity requirements. Electrolytes need to be dense and non-porous to prevent short circuits, and they must possess high ionic conductivity for oxygen ions to travel from the cathode to the anode. The anode needs to be very porous to allow the fuel to flow towards the electrolyte (i.e. mass transport). The cathode also needs to be porous in order to allow oxygen molecules to reach the electrode/electrolyte interface. It is typically considered desirable to grade the porosity of electrodes to increase the SOFC performance. Large open porous electrode structures are desired near the gas channel to enhance mass transport, whereas, smaller-sized pores are desired near the electrolyte to enhance molecular diffusivity and electrochemical activity. This in turn creates higher power density and power output.

1.3 SOFC FABRICATION METHODS

1.3.1 Traditional approaches

SOFC's have traditionally been made using adaptations to both thick film and thin film processing techniques.

The common thick film approaches include tape casting, tape calendaring, screen printing and wet spraying where fabrication is usually carried out in layers. It is then followed by firing at high temperatures (1300 ºC-1700 ºC).

Thin film deposition approach that have been used to form cell components include chemical and physical process such as chemical vapor deposition (CVD), plasma spraying (PS) and spray pyrolysis [6][7].

These conventional methods are not particularly well suited for precise local control of chemical composition and/or structure. Thus, there is a need to explore alternative fabrication methods. The research described here employs 3D direct write printing to allow chemical

composition and structure of a SOFC to be precisely engineered. This allows one to locally control the size and shape of pores in the anode and cathode layers and hence the resulting porosity. The method used for this research is a form of additive manufacturing that utilizes micro-dispensing technology. This method allows one to control the material deposition rate and path simultaneously. This is a major advantage of this process over various more traditional fabrication processes. The direct-write technique is also capable of grading porosity/composition within a layer in addition to grading porosity in successive layers.

1.3.2 3D Direct Write Methods

For this research, an nScrypt Tabletop series microdispensing system with a SmartPump has been utilized for fabrication (Figure 2). The fuel cell material is introduced in a slurry form (referred to as paste or ink), and the tool is capable of printing highly viscous materials up to 1 Million cP. For fabrication, component geometry can be imported from Computer Aided Design (CAD) software, such as ProEngineer or Solidworks. Alternatively, input can be provided in the form of machine code. For a CAD file, a part is built layer-by-layer from the bottom up. Any pattern can be printed in the XY plane or raised into the Z plane for a conformal surface. [8]

a) nScrypt Benchtop Model

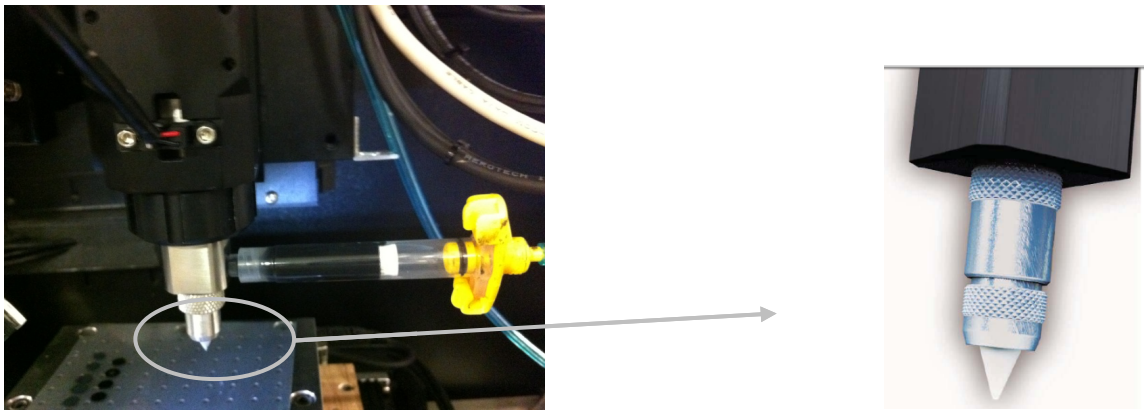

b) Smart Pump setup

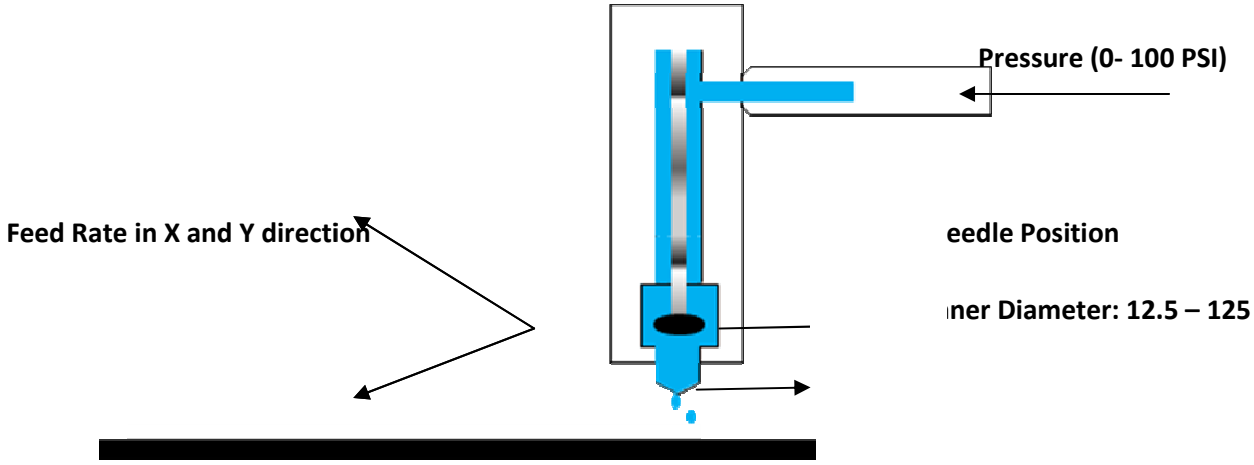

c) Schematics of a Smartpump

Figure 2 a) nScrypt Benchtop Model b) SmartPump setup c) Schematics of a Smart pump

The SmartPump is a precise micro-dispensing pump that consists of a positive pressure pump with a computer-controlled needle valve. The SmartPump can control starts and stops as well as material flow rate for a large range of ink viscosities. The computer-controlled needle valve provides active valving to control flow characteristics and includes opening, closing and suck-back. The dead volume inside the SmartPump ranges from 0.025 cc to 0.1 cc. With these features and degree of control, it is possible to dispense very small volumes of material down to 20 picoliters and a range of viscosities from 1 centipoise to over 1,000,000 centipoise. [8]

Once the SmartPump is setup as shown in Figure 2(b), air pressure (0-100 PSI) is applied to the 3cc syringe barrel containing the ink. The pressure pushes the ink into the main valve body. The valve opening is then regulated to control the amount of ink going to the ceramic nozzle. Ceramic nozzles are available with diameters ranging from 12.5 – 125 µm. The material comes out through a nozzle as shown in Figure 2(c).

This method is flexible with regard to materials and part geometry. DW printing processes can print micro lines, dots, three-dimensional printed structures as well as conformal patterns that follow a 3D contoured surface. The process has a wide range of applications including printed conductors, resistors, optics, adhesives, sealants, frit, solders, encapsulants, wire bonding, underfilling, flip-chip bumping, MEMS, etc.

CHAPTER 2: LITERATURE REVIEW

This chapter is broken into seven sections and provides literature review on SOFC, advantage of SOFC, disadvantages of SOFC, materials use in SOFC, applications of fuel cells, fabrication methods for SOFC and the problems faced by SOFC technology.

2.1 SOLID OXIDE FUEL CELLS

A fuel cell is a device that generates electricity by a chemical reaction. Every fuel cell consists of an anode, cathode and electrolyte layer. The cathode and anode serve as electrodes, one positive and one negative, respectively. The reactions that produce electricity take place at the electrodes. The electrolyte transports ions from one electrode to the other. Typically, hydrogen is the basic fuel, however fuel cells also require oxygen. A single fuel cell generates a small amount of direct current (DC) electricity. Thus, individual cells are typically assembled into a stack to generate sufficient electricity for the application. The common types of fuel cells are phosphoric acid (PAFC), molten carbonate (MCFC), proton exchange membrane (PEM) and solid oxide fuel cells (SOFC), all named after their electrolytes [9][10]. Table 1 provides a comparison between various fuel cell technologies.

Table 1 Comparison of Fuel Cell Technologies [10]

Comparison of Fuel Cell Technologies

DOE Hydrogen Program

Fuel Cell Type	Common Electrolyte	Operating Temperature	System Output	Electrical Efficiency	Combined Heat and Power (CHP) Efficiency	Applications	Advantages
Polymer Electrolyte Membrane (PEM)*	Solid organic polymer poly-perfluorosulfonic acid	50 - 100°C 122 - 212°F	<1kW – 250kW	53-58% (transportation) 25-35% (stationary)	70-90% (low-grade waste heat)	▪ Backup power ▪ Portable power ▪ Small distributed generation ▪ Transportation ▪ Specialty vehicles	▪ Solid electrolyte reduces corrosion & electrolyte management problems ▪ Low temperature ▪ Quick start-up
Alkaline (AFC)	Aqueous solution of potassium hydroxide soaked in a matrix	90 - 100°C 194 - 212°F	10kW – 100kW	60%	>80% (low-grade waste heat)	▪ Military ▪ Space	▪ Cathode reaction faster in alkaline electrolyte, leads to higher performance ▪ Can use a variety of catalysts
Phosphoric Acid (PAFC)	Liquid phosphoric acid soaked in a matrix	150 - 200°C 302 - 392°F	50kW – 1MW (250kW module typical)	>40%	>85%	▪ Distributed generation	▪ Higher overall efficiency with CHP ▪ Increased tolerance to impurities in hydrogen
Molten Carbonate (MCFC)	Liquid solution of lithium, sodium, and/or potassium carbonates, soaked in a matrix	600 - 700°C 1112 - 1292°F	<1kW – 1MW (250kW module typical)	45-47%	>80%	▪ Electric utility ▪ Large distributed generation	▪ High efficiency ▪ Fuel flexibility ▪ Can use a variety of catalysts ▪ Suitable for CHP
Solid Oxide (SOFC)	Yttria stabilized zirconia	600 - 1000°C 1202 - 1832°F	<1kW – 3MW	35-43%	<90%	▪ Auxiliary power ▪ Electric utility ▪ Large distributed generation	▪ High efficiency ▪ Fuel flexibility ▪ Can use a variety of catalysts ▪ Solid electrolyte reduces electrolyte management problems ▪ Suitable for CHP ▪ Hybrid/GT cycle

**Direct Methanol Fuel Cells (DMFC) are a subset of PEM typically used for small portable power applications with a size range of about a subwatt to 100W and operating at 60 - 90°C.*

For print copies of this fact sheet, please call the DOE Energy Efficiency and Renewable Energy Information Center at 877-EERE-INF(O)/877-337-3463. December 2008

SOFC's use a hard and non-porous ceramic compound as the electrolyte, and they operate at very high temperatures (~1000°C). The two most common design configurations for SOFC's are the planar design and the tubular design shown in Figure 3. In a planar design, the components are assembled in flat stacks. The air and fuel flow through channels built into the interconnect and/or the cathode and anode. In the tubular design, components are assembled in concentric rings around a hollow tubular cathode. Air flows through the tube, and fuel flows over the exterior surface as shown in Figure 3(b) [11]. Tubular SOFC designs are closer to commercialization and are being produced by several companies around the world. SOFC's are suitable for stationary applications as well as for auxiliary power units used in vehicles to power electronics [12].

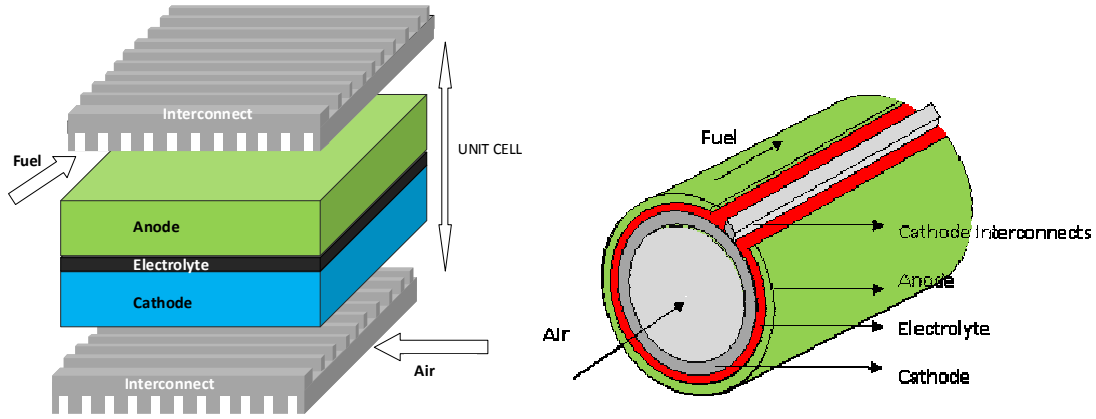

a) Planar SOFC **b) Tubular SOFC**

Figure 3 Configuration for a planar design SOFC and tubular design SOFC

There are 3 primary configurations for self-supporting planar SOFC's: electrolyte-supported cells, cathode-supported cells and anode-supported cells. Electrolyte-supported SOFC's utilize a thick electrolyte layer (100-200µm) and 30-100 µm thick electrodes. They typically exhibit high ohmic resistance and low polarization concentration for both the anode and the cathode. Cathode-supported cells exhibit lower ohmic losses due to the thinner electrolyte, high anode polarization concentration and low cathode polarization concentration. The anode supported cell is the most commonly used self-supported structure. The thick anode (500-1000µm) supporting a thin (5-50µm) electrolyte and cathode exhibits low ohmic resistance and low cathode polarization concentration. The anode exhibits lower polarization concentration when compared to cathode-supported cells.

Fuel cell systems typically use pure hydrogen as a fuel, but SOFC's can use hydrogen or other forms of fuels such as methane, butane, natural gas, diesel, gasoline, etc. During operation, the fuel (assuming the fuel is hydrogen) passes over the anode which oxidizes the H_2 molecules under high temperature, thus producing electrons that are free to do work. For each H_2 molecule, two electrons are created. On the cathode side, high-temperature oxygen is blown across the

cathode where it is reduced to negatively charged ions. Each oxygen (O_2) molecule catalytically acquires 4 electrons and splits into two oxygen ions as shown in Table 2. These oxygen ions are conducted through the electrolyte membrane where they then combine with hydrogen on the anode side. The products of this cycle are electric current, water and heat. When a load is connected between the anode and cathode, an electric circuit is created. Each cell typically produces little more than one volt, so individual cells are assembled in layers/stacks to generate a useful voltage. Figure 4 provides a visual summary of a SOFC during operation. The basic chemical reactions in a SOFC running on hydrogen fuel during the operation are shown below [12] [13].

Table 2 Chemical Reactions of a SOFC

Anode Reaction:	$2\ H_2 + 2\ O^{2-} \Rightarrow 2\ H_2O + 4\ e^-$
Cathode Reaction:	$O_2 + 4\ e^- \Rightarrow 2\ O^{2-}$
Overall Cell Reaction:	$2\ H_2 + O_2 \Rightarrow 2\ H_2O$

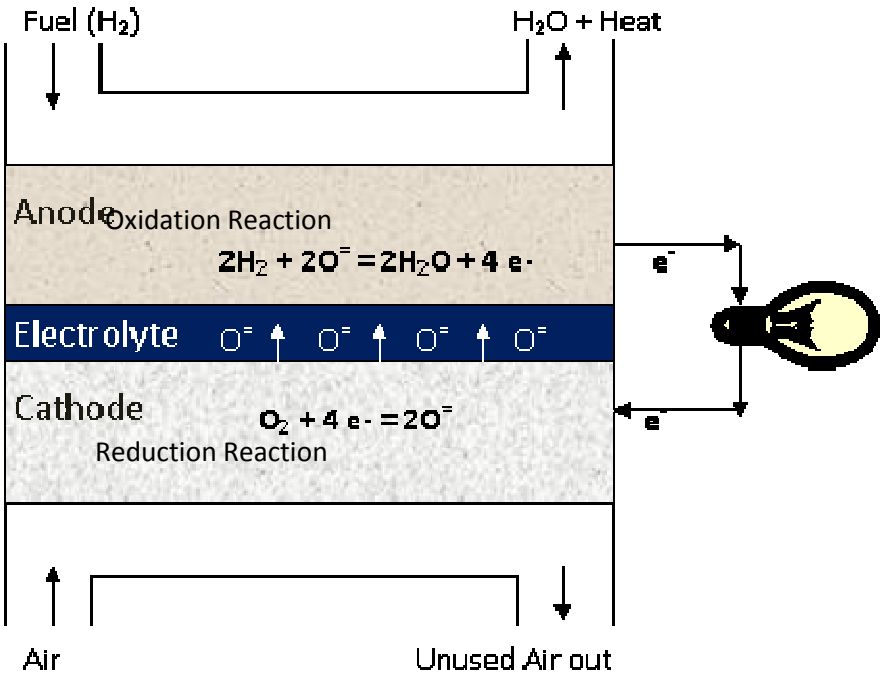

Figure 4 SOFC Operating Concept

2.2 ADVANTAGES OF SOFC

A fuel cell generates electricity by an electrochemical process which offers many advantages over traditional energy conversion systems including higher efficiency, reliability, modularity, fuel adaptability and lower emissions.

Fuel cells running on pure hydrogen theoretically produce zero-emissions. Even with other forms of fuel, they produce very low levels of nitrogen oxides (NO_x), sulfur oxides (SO_x) and much lower levels of carbon dioxide (CO_2) compared to conventional power sources. NO_x is the main constituent of acid rain and photochemical smog. SOFC's can significantly reduce pollution caused by combustion of fossil fuels. The only byproduct is water and heat. The waste heat can be captured for beneficial purpose (co-generation). Fuel cells are also very quiet, which reduces noise pollution. Fuel cell power plants qualify under several environmental certifications established by the government, such as the Leadership in Energy and Environmental Design

(LEED) program and Renewable Energy Standards (RES). This makes them eligible for significant financial incentive programs. Fuel cell energy power plants can reduce emissions generated by fossil-fuel-based backup generators [12][13][14].

The South Coast Air Quality Management District found that a fuel cell power plant running on natural gas emits 98% fewer nitrogen oxides than the district's own tough standard. Successful implementation of fuel cells in transportation could potentially take the automobile out of the climate change debate. Fuel cell power plants are so clean that some cities have exempted the technology from air permit requirements. A program to install eight fuel cells is well underway at wastewater treatment plants around New York City. They are expected to eliminate nearly 170 tons of regulated emissions and more than 9,000 tons of carbon dioxide, and to reduce fuel oil consumption by 3,000 barrels per year. A fuel cell power plant may create less than one ounce of pollution per 1,000 kilowatt-hours of electricity produced, compared to the 25 pounds of pollutants for conventional combustion generating systems as shown in Figure 5. [12][13][14].

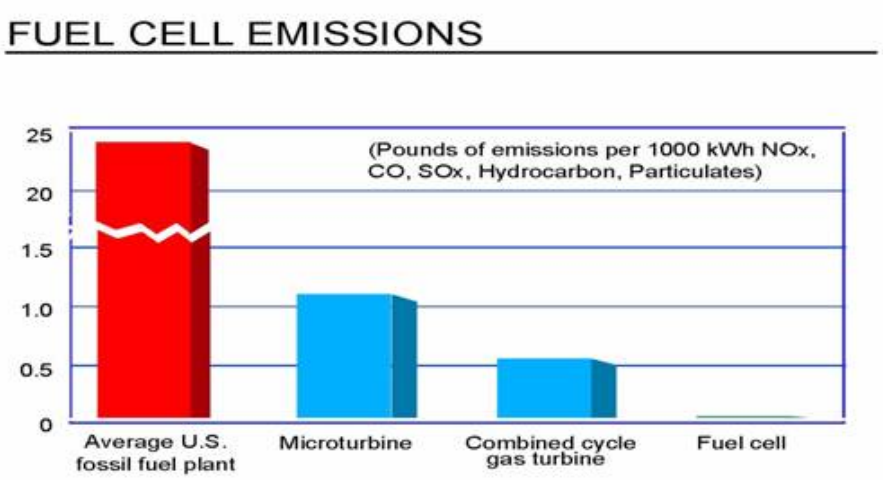

Figure 5 Fuel cell emissions comparisons [14]

Typically fuel cells run on hydrogen and will continue to generate power as long as fuel is supplied. SOFC's can use a wide variety of fuels: fossil fuels, such as natural gas and coal;

alcohol fuels, such as methanol or ethanol; hydrogen compounds containing no carbon, such as ammonia or borohydride; or biomass, methane, landfill gas or anaerobic digester gas from wastewater treatment plants. SOFC's can be instrumental in renewable energy systems, as they have the ability to harness energy from bio-gases generated from industrial and agricultural plants, landfills and waste water treatment. This characteristic qualifies them for financial incentives in certain areas. In some places where digester gas production volume is variable, fuel cell plants are designed to operate through automatic blending with natural gas [13][14].

The U.S. consumes approximately 21 million barrels of oil per day, but the domestic production is only 6 million barrels per day. Hence, the majority of oil consumed in the United States is imported. The cost to import oil is approximately $410 billion dollars a year. SOFC's or any other fuel cells do not require conventional fuels such as oil and can therefore reduce economic dependence on foreign countries. [12]

Fuel cell energy production can be located on-site (i.e. distributed power generation), in which case the users are assured of increased reliability. This is a necessary requirement for applications such as hospitals, universities and manufacturing facilities. Fuel cell energy production can operate independently of the grid, and have an availability of 95% compared to 35% for wind and solar technologies. The National Power Laboratory estimates that the typical computer location experiences 289 power disturbances a year that are outside the voltage limits of the computer equipment, causing U.S. businesses to lose $29 billion annually. Fuel cells may help prevent loss of power and the resulting damage. Fuel cells offer clean, high quality power, crucial to an economy that depends on increasingly sensitive computers, medical equipment and machines. A fuel cell does not run down or require recharging. As long as fuel is supplied, it will produce energy in the form of electricity and heat [12][13][14].

The only moving parts in fuel cells are involved with water, heat and air management (i.e. pumps, blowers and compressors). When compared to internal combustion engines, there are significantly fewer moving parts that require maintenance. This in turn reduces the operating costs. Fuel cells can also be monitored remotely and any problems dealt with quickly [15].

Fuel cells are also very versatile. They can be stacked to generate the desired power output and are capable of achieving outputs in the megawatt range. Fuel cells are very quiet, so they can be placed close to businesses or residences where noise pollution is undesirable. The use of smaller stationary fuel cells can lead to a more stabilized and decentralized power grid [15].

Fuel cells have a higher efficiency than diesel or gas engines. Fuel cells are typically 2-3 times as efficient as internal combustion engines for vehicle transportation which operate at only 10-16% efficiency. A fossil fuel powered plant operates at about 35% electrical generation efficiency. Fuel cell power generation systems in operation can achieve 40% to 50% electrical generation efficiency utilizing hydrocarbon fuels [15]. Fuel cell power plants generate more electricity per unit of fuel than almost any other distributed energy source. Fuel cell power plants can achieve efficiency of over 80% if used in co-generation applications.

SOFC's operate at high temperatures for increased efficiencies, which can reduce the need for expensive precious metals used in other cell types. The high temperatures require longer start up times though, so SOFC's are better suited for continuous operation rather than intermittent operation. SOFC's exhibit fuel efficiencies up to 70%. If combined with heat recovery technologies, a total system efficiency of up to 85% can be achieved [13]. The table below compares tubular SOFC systems with other fuel cell systems and other generation options.

Table 3 Comparison of tubular SOFC systems with other fuel cell systems [13]

	PEM	PAFC	MCFC	SOFC	Micro-GT	Diesel Engine	Stirling Engine
Electrical efficiency using natural gas (net AC/LHV), %	35	40	45-50	45-50*	30	35	30
Performance degradation, %/1000 hrs	>1	0.44	0.60	<0.10	0.20	0.20	na
Emissions using natural gas: NOx, g/MWh	<20	<10	<10	<10	300	700	200
SOx, g/MWh	<0.1	<0.1	<0.1	<0.1	1	1	1
Noise, dBA @ 10 m <60	<60	60	65	65	65	80-90	60
Water consumption, gal/MWh	0	90	88	0	0	0	0
Total fuel efficiency using natural gas (net AC/LHV), %	35	65	70	80-85	~75	~78	~77

Overall, SOFC's produce near zero emissions, allow for fuel flexibility, are efficient, operate quietly and require low maintenance compared to many existing technologies.

2.3 DISADVANTAGES OF SOFC

There are several obstacles that need to be overcome before widespread use of SOFC's occurs. The biggest disadvantage for any fuel cell type is the cost. There are some SOFC systems in use today, but relatively few are cost effective. For stationary fuel cells, typical capital costs for installed systems exceed $5,000 per kilowatt, well above the target capital cost of $1,000-$1,500 used by most energy generation developers [15]. Thus, there is also an issue of economic feasibility [10].

Fuel cells are still in a relatively early stage of development, and commercially available systems are limited. This emerging technology requires risk-taking early adopters as end users in order to ultimately expose more consumers to the benefits of fuel cells. In order to become widely accepted as a clean distributed generator of energy, fuel cells must prove their adaptability for a variety of applications. Fuel cell systems also need to have a longer lifespans or be easily and cheaply replaced [10].

In addition to the above issues, the high-temperature operation of SOFC's has other disadvantages. It results in a slow start-up and requires significant thermal shielding to retain heat and protect personnel. This is suitable for utility applications, but not for transportation and small portable applications. As for car makers who are looking to use fuel cell energy, fuel cell-powered cars can take longer to fuel and drive shorter distances than other cars, which is a major issue that needs to be addressed. The high operating temperatures also place stringent durability requirements on materials used for the anode, cathode, electrolyte and interconnect [10].

Fuel cells are also categorized as energy losers. It can end up costing more to produce hydrogen energy than what is earned by using hydrogen in fuel cells. Fueling these fuel cells is still a problem since the production, transportation, distribution and storage of hydrogen is a difficult issue. Hydrogen is expensive to produce: it takes 1,600 joules to produce an amount of hydrogen yielding only 1,000 joules, while it takes only 167 joules to produce an amount of gasoline yielding 1,000 joules [10]. The current method (electrolysis and reforming) of producing hydrogen produces greenhouse gases. In the long term, wind energy can tap hydrogen from water in the ocean. In the short run, it is likely to come from reformed natural gas which is currently the cheapest and most efficient way to make hydrogen. The potential for SOFC's to directly operate on multiple hydrocarbon sources in addition to pure hydrogen can alleviate this

problem. They can operate using other forms of fuel: fossil fuels, such as natural gas and coal; alcohol fuels, such as methanol or ethanol; from hydrogen compounds containing no carbon, such as ammonia or borohydride; or from biomass, methane, landfill gas or anaerobic digester gas from wastewater treatment plants [10][15].

2.4 MATERIALS IN SOFC

The selection of materials for the four components (anode, cathode, electrolyte and interconnect) of a SOFC is a challenge. SOFC's operates at high temperatures (700°C - 1000 °C) in order to achieve sufficiently high current densities and power output. The material for each of the components must therefore be able to withstand operation at these high temperatures. Each component's material must have the conductive properties required to perform its function in the cell. Since the components are stacked, reactivity and inter-diffusion between the components must be kept to a minimum. The thermal expansion coefficients of the components must be as close to one another as possible in order to minimize thermal stresses which could lead to cracking and warping [11][16].

The electrolyte material must have very high ionic conductivity and virtually no electronic conductivity, so that the oxygen ions can easily diffuse through the electrolyte membrane. It must be fully dense so that reactant gases from the anode and cathode sides do not pass through it. The electrolyte should also be as thin as possible to reduce the distance oxygen ions have to travel to get to the anode. This minimizes ohmic/resistive losses in the cell. Yttria-stabilized zirconia (YSZ) and doped cerium oxides are the two most common materials used for SOFC electrolytes [9][11][16]. Table 4 summarizes the advantages and disadvantages of various electrolyte materials in a SOFC [17]. A list of other commonly used SOFC materials sold by Sigma-Aldrich is tabulated in Table 5.

Table 4 Advantages and disadvantages of possible electrolyte candidates for SOFC [17]

YSZ (Yttria-stabilized zirconia)	GCO (Gadolinium doped ceria)	LSGM (Lanthanum Strontium Gallate Magnesite)	ScSZ (Scandia-doped zirconia)
Excellent stability in oxidizing and reducing environment	Good compatibility with cathode materials	Good compatibility with cathode materials	Excellent stability in oxidizing and reducing environment
Excellent mechanical stability (3YSZ)	Mixed electronic-ionic conductor at low pO_2 (application in anode cermets)		Better long term stability than 8YSZ?
> 40,000 h of fuel cell operation possible	Electronic conduction at low pO_2→low OCV	Ga-evaporation at low pO_2•Incompatable with NiO	Availability and price of scandium
High quality raw materials available	Mechanical stability	Mechanical stability	
Low ionic conductivity (especially 3YSZ)			
Incompatible with some cathode materials			

Table 5 Sigma-Aldrich materials for SOFC applications

Materials Description	Composition
Anode Materials	
Nickel oxide - Cerium samarium oxide for coatings, NiO/SDC, ≥99% trace metals basis	$(CeO_2$-$Sm_2O_3)$, 40 wt. % NiO, 60 wt. %
Nickel oxide - Yttria-stabilized zirconia ≥99%, general applications, NiO/YSZ	NiO, 60 wt. % Y_2O_3-ZrO_2, 40 wt. %
Nickel oxide - Yttria-stabilized zirconia for coatings, NiO/YSZ	$(Y_2O_3$-$ZrO_2)$, 34 wt. % NiO, 66 wt. %
Nickel(II) oxide 99.99% trace metals basis	NiO
Vanadium(III) oxide 99.99% trace metals basis	V_2O_3
Vanadium(V) oxide 99.99% trace metals basis	V_2O_5
Cathode Materials	
Lanthanum nickelate, strontium doped nanopowder, <100 nm particle size (BET)	$La_{1.6}Sr_{0.4}NiO_4$
Lanthanum nickelate nanopowder, <100 nm particle size (BET)	La_2NiO_4
Lanthanum strontium cobalt ferrite LSCF 6428	$La_{0.6}Sr_{0.4}Co_{0.2}Fe_{0.8}O_3$
Lanthanum strontium cobalt ferrite composite cathode powder, LSCF/GDC	$Ce_{0.9}Gd_{0.1}0_2$, 50 wt. % $La_{0.6}Sr_{0.4}Co_{0.2}Fe_{0.8}O_3$, 50 wt.
Lanthanum strontium cobalt ferrite powder, <0.5 μm particle size	$La_{0.6}Sr_{0.4}Co_{0.2}Fe_{0.8}O_3$
Lanthanum strontium ferrite powder, <0.5 μm particle size	$La_{0.6}Sr_{0.4}FeO_3$
Lanthanum strontium manganite LSM-20, ≥99%	$La_{0.8}Sr_{0.2}MnO_3$
Lanthanum strontium manganite LSM-35	$La_{0.65}Sr_{0.35}MnO_3$
Lanthanum strontium manganite composite cathode powder, LSM-20/GDC10	$Ce_{0.9}Gd_{0.1}O_2$, 50 wt. % $La_{0.8}Sr_{0.2}MnO_3$, 50 wt. %
Lanthanum strontium manganite composite cathode powder, LSM-20/YSZ, ≥99%	$(Y_2O_3)_{0.08}(ZrO_2)_{0.92}$, 50 wt. %
Manganese cobalt oxide spinel, powder, <0.5 μm particle size	$Mn_{1.5}Co_{1.5}O_4$

Electrolyte Materials	
Cerium oxide, praseodymium doped nanopowder, <100 nm particle size	$Ce_{0.8}Pr_{0.2}O_2$
Cerium(IV) oxide-calcium doped nanopowder	$Ce_{0.9}Ca_{0.1}O_2$
Cerium(IV) oxide-gadolinium doped <0.5 µm particle size, powder, contains 10 mol % gadolinium as dopant	$Gd_{0.1}Ce_{0.9}O_{1.95}$
Cerium(IV) oxide-gadolinium doped nanopowder, contains 10 mol % gadolinium as dopant	$Ce_{0.9}Gd_{0.1}O_2$
Cerium(IV) oxide-gadolinium doped nanopowder, contains 20 mol % gadolinium as dopant	$Ce_{0.8}Gd_{0.2}O_2$
Cerium(IV) oxide-samarium doped <0.5 µm particle size, powder, contains 20 mol % samarium as dopant	$Sm_{0.2}Ce_{0.8}O_{1.9}$
Cerium(IV) oxide-samarium doped nanopowder, contains 15 mol % samarium as dopant	$Ce_{0.85}Sm_{0.15}O_2$
Cerium(IV) oxide-gadolinium doped nanopowder, contains 20 mol % gadolinium as dopant	$Ce_{0.8}Gd_{0.2}O_2$
Cerium(IV) oxide-samarium doped <0.5 µm particle size, powder, contains 20 mol % samarium as dopant	$Sm_{0.2}Ce_{0.8}O_{1.9}$
Cerium(IV) oxide-samarium doped nanopowder, contains 15 mol % samarium as dopant	$Ce_{0.85}Sm_{0.15}O_2$
Cerium(IV) oxide-gadolinium doped nanopowder, contains 20 mol % gadolinium as dopant	$Ce_{0.8}Gd_{0.2}O_2$
Cerium(IV) oxide-samarium doped <0.5 µm particle size, powder, contains 20 mol % samarium as dopant	$Sm_{0.2}Ce_{0.8}O_{1.9}$
Cerium(IV) oxide-samarium doped nanopowder, contains 15 mol % samarium as dopant	$Ce_{0.85}Sm_{0.15}O_2$
Cerium(IV) oxide-yttria doped nanopowder	$Ce_{0.85}Y_{0.15}O_2$
Zirconium(IV) oxide-yttria stabilized nanopowder	$(ZrO_2)_{0.97}(Y_2O_3)_{0.03}$
Zirconium(IV) oxide-yttria stabilized nanopowder	$(ZrO_2)_{0.92}(Y_2O_3)_{0.08}$
Zirconium(IV) oxide-yttria stabilized nanopowder, <100 nm particle size (BET)	$(Z_rO_2)_{1-x}(Y_2O_3)_x$
Zirconium(IV) oxide-yttria stabilized submicron powder, 99.5% trace metals basis (purity excludes ~2% HfO_2)	$(ZrO_2)_{0.947}(Y_2O_3)_{0.053}$
Zirconium(IV) oxide-yttria stabilized submicron powder, 99.9% trace metals basis (purity excludes ~2% HfO_2)	$(ZrO_2)_{0.92}(Y_2O_3)_{0.08}$

For zirconia based SOFC's, the cathodes are commonly made from lanthanum manganate ceramics doped with strontium (LSM) because of its compatibility with the YSZ electrolyte. Its coefficient of thermal expansion (CTE) must closely match that of YSZ. Cathodes need to be electrically conductive, porous and have properties that can withstand operation in a reducing environment.

Anodes need to have properties similar to those of the cathode except that the material must have properties to withstand operation in an oxidizing environment. Anodes need to have electronic conductivity, have a CTE that is compatible with the electrolyte, and they need to be porous. Nickel (Ni) is a commonly used material for anodes due to its abundance and affordability. The most common anode is made out of a NiO-YSZ composite, where YSZ

provides structural support for the Ni particles. It also improves adhesion of the anode to the electrolyte [11][16].

Interconnects are used to physically separate one cell from the other and to electrically connect each cell in series so that the electricity generated by each cell can be combined as shown in Figure 3. It is exposed simultaneously to both the reducing and oxidizing environment of the cell. Interconnects must exhibit very high electrical conductivity, should remain impermeable to gases to avoid mixing of fuel and oxygen directly, must have a CTE that closely matches both the electrodes and the electrolyte, and must be chemically inert with respect to the other fuel cell components. In a SOFC, doped lanthanum chromite is often used as the interconnection for cells intended for operation at about 1000^{o}C [18]. In many cases, interconnects are applied to the anode by plasma spraying. Then the entire cell is co-fired [9][11][16]. A summary of desired properties and processing requirements for SOFC component layers are tabulated below in Table 6 [19].

Table 6 Micro-structural and property of SOFC component layers [19]

	Anode	Electrolyte	Cathode	Interconnect
Microstructure	Porous, many triple-phase boundaries, stable to sintering.	Dense, thin, free of cracks and pinholes.	Porous, many triple-phase boundaries, stable to sintering.	Dense separation between cells, porous or channeled gas transport paths.
Electrical	Electronically and preferably ionically conductive.	Ionically but not electronically conductive.	Electronically and preferably ionically conductive.	Electronically but not ionically conductive; conductive oxide layer.
Chemical	Stable in fuel atmosphere; preferably also stable in air for redox tolerance. Catalytic for oxidation and reforming but not for carbon deposition.	Stable in both oxidizing and reducing environment. Minimal reduction and resulting electronic conductivity in reducing conditions.	Stable in air environments. Catalytic for oxygen reduction. Resistant to performance loss caused by chromium deposition.	Stable in both air and fuel environments. Resistant to rapid oxidation. Minimal chromium evaporation.
Thermal Expansion	Compatible with other layers, especially electrolyte.	Compatible with other layers, especially structural support layer.	Compatible with other layers, especially electrolyte.	Compatible with other layers, especially electrolyte.
Chemical Compatibility	Minimal reactivity with electrolyte and interconnect.	Minimal reactivity with anode and cathode.	Minimal reactivity with electrolyte and interconnect.	Minimal reactivity with anode and cathode.

2.5 APPLICATIONS OF FUEL CELLS

There are many applications for fuel cells. Fuel cells are increasingly being used to power trucks, buses, boats, trains, planes, scooters, forklifts and bicycles. There are also fuel cell powered vending machines, vacuum cleaners and highway road signs. Miniature fuel cells for applications with cellular phones, laptop computers and portable electronics are under research and commercialization. Some hospitals, credit card centers, police stations and banks are using fuel cells to provide power to their facilities. Wastewater treatment plants and landfills are using

fuel cells to convert the methane gas they produce into electricity. Telecommunications companies are installing fuel cells at cell phone, radio and 911 towers [14].

Many of the major automakers are working aggressively to commercialize a fuel cell vehicle. Fuel cell based vehicles produce almost zero carbon emissions and have a higher rate of energy efficiency than vehicles based on internal combustion technology. Vehicle manufacturers, such as DaimlerChrysler, Ford, General Motors, Honda and Toyota are actively researching and developing transportation fuel cells for future use in cars, trucks and buses. There are already hydrogen powered cars on the street today, such as HONDA FCX Clarity, Premacy Hydrogen RE Hybrid, Mazda RX-8 Hydrogen RE, etc. These manufacturers are also targeting buses, trucks and ships to be powered by fuel cells. Toyota's FCHV-BUS and Mercedes-Benz (Daimler AG) Citaro bus are already in use. Also, the Type 212 submarines used by the German and Italian Navy's use fuel cells to remain submerged for weeks without the need to surface.

Portable SOFC's are small and contained and can be designed for a variety of purposes. These units can provide back-up electrical generation for military, temporary or special needs applications. As technology advances and fuel cells become smaller, the potential applications for portable fuel cells are limitless. Laptop computers, cellular phones, video recorders and hearing aids could potentially be powered by portable fuel cells [13]. The Spanish company Jofemar sells Vision Multiseller H2, an autonomously powered vending machine that runs on hydrogen.

Another area where fuel cell technology is heavily pursued is for Auxiliary Power Units (APUs). APU's need to be relatively small, light and durable. The specifications for this application are approximately 3kW to 5kW, 42 VDC, 50 kg and 50 liters. Price projections range from USD 200-1000. Large market potentials have been forecast for APUs in long-haul trucks

and busses for supplying air conditioning and other electrical services without the need to idle a large diesel engine, thereby reducing pollution and increased fuel savings.

Delphi, a leading global supplier of electronics and technologies for automotive, commercial vehicles and other market segments, is focusing on the development of SOFC's that generate electric power for commercial vehicles, stationary power generation and military applications.

SOFC's have advantages over battery-electric vehicles, which require recharging that takes time and electricity. Fuel cell-based vehicles can be refueled quickly at a filling station just like gasoline cars. However, manufacturers must overcome certain challenges, such as the issue of storing hydrogen gas onboard vehicles, the availability of hydrogen filling fuel stations, generation of hydrogen, transportation of hydrogen to fueling stations, getting people to drive hydrogen based vehicles, etc [13]. Another influential factor is the susceptibility of funding for fuel-cell technology to change with different political administrations.

Last, industrial applications for stationary power generation represent the first area of significant market penetration for fuel cell systems. The advantage of stationary fuel cell systems is that they could provide a clean source of on-site power to a variety of end users (manufacturing facilities, hospitals, universities, airports, etc.). In 1999, the First National Bank of Omaha (FNBO) installed a 800-kW fuel-cell system as the primary power source for its 200,000 square foot Technology Center's critical loads. There are more than 250 stationary fuel cell systems generating power for industrial applications around the world. The majority of them are PAFC's, but there are also SOFC, MCFC, and PEM fuel cell installations in operation. They are designed for installation in permanent settings such as hospitals, banks, airports, military bases, and universities [13].

A market research report, "Global Fuel Cell Market by Technology, Application, Component, Installation, Cost, Geography, Trends and Forecasts (2011 - 2016)," by MarketsandMarkets predicts that the global fuel cell market will reach $1.6 billion from an estimated $240 million in 2010 with CAGR of 17.6 percent during 2011 - 2016. In 2010, the global fuel cell market was valued at $650 million with 0.14 million unit shipments and is estimated to reach $1.6 billion in 2016. Also by 2016, annual fuel cell shipments will reach 10 million units from 0.14 million units in 2010 with a CAGR of 115% during 2011 – 2016. In terms of MW capacity, those 10 million units will be equivalent to 3,760 MW compared to a mere 240 MW in 2010. Other various market research reports predict similar trends of drastic increases in fuel cell technology and an increase in market value.

The market share that will belong to SOFC's is unclear, but it will be significant. SOFC's are primarily targeted for use in three energy applications: stationary energy sources (residential, CHP and DG, base load), transportation (automobile, truck and aircraft auxiliary power units) and military applications (soldier power, battery charger) [11] [12] [14].

2.6 FABRICATION of SOFC's

Traditionally there have been two common fabrication approaches for making SOFC's. One approach is based on thick film deposition techniques whereas the other is based on thin films deposition techniques (vapor or spray deposition techniques). The common thick film approaches include tape casting, tape calendaring, screen printing and wet spraying. Fabrication is carried out in layers and is then followed by sintering at high temperatures (1300ºC - 1700ºC). The vapor/spray deposition approaches involve formation of cell components on a support by chemical and physical processes such as chemical vapor deposition, plasma spraying, dip coating and spray pyrolysis [6] [7].

2.6.1 Tape Casting and Freeze Tape Casting

The tape casting method is used for the production of thin and wide ceramic tapes from ceramic slurry. The slurry is created by mixing the ceramic powder, an ink vehicle and additives. The ceramic slurry is spread across the tape bed (conveyer belt) where a doctor blade helps to form a flat and even layer. The layer is then dried and ready for post-processing.

This process is extensively used in fabrication of SOFC structures, the electrodes and the electrolyte. The tape casting method with a co-firing process has been successfully applied to fabricate an anode-supported electrolyte for the SOFC unit cell [20]. A planar anode-supported electrolyte has been fabricated using a tape casting method that involved a single step co-firing process. A thin 10 µm layer of dense electrolyte on a NiO/YSZ cermet anode without warpage has been fabricated with this method [4][21].

A modified version of the tape casting process, called freeze tape casting (FTC), has being investigated for fabrication of SOFC's (Figure 6). When an aqueous sol of particles is tape cast on a suitably cold substrate, the thick film freezes. The freezing process entails nucleation and growth of ice crystals. The growth and expansion of ice particles force the solid particles to interact with each other in the inter-dendritic regions between the ice crystals, thereby causing local concentration of solid particulates. When the ice crystals are removed by a subsequent freeze drying process, the solid particles remain intact. The freeze dried thick film is then sintered in a conventional furnace. The void space left by the volume formerly occupied by the ice crystals leads to a porous structure. In this process, porosity can be tailored through choice of the liquid vehicle, the concentration of suspended ceramic particles, the freezing temperature set point, and time on the cold bed [22][23].

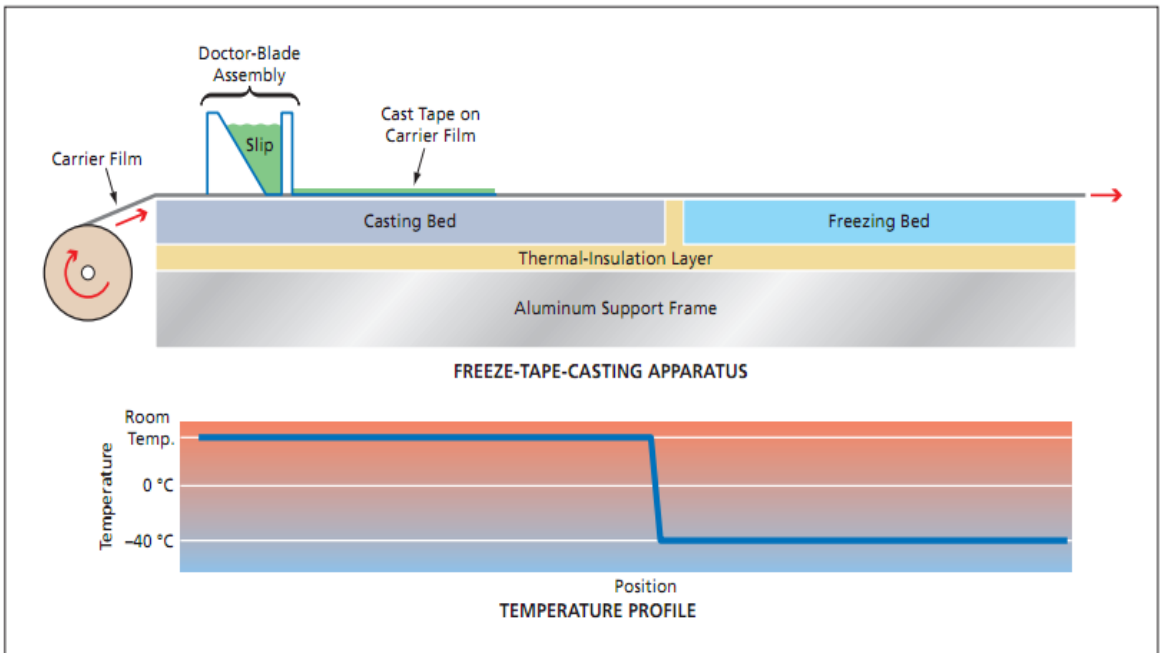

Figure 6 Freeze Tape Casting Process [23]

Functionally graded and continuously aligned pore structures have also been successfully fabricated by an FTC process for use in SOFC's. The FTC process provides a direct means of forming and controlling complex pore structures in a ceramic part [24]. A study conducted to fabricate porous alumina sintered bodies by a Gelate-Freezing method showed that different pore size and porosity could be controlled through proper selection of the alumina and water content in the slurry, the cooling temperature and the casting direction. Pore size and porosity can be controlled by the alumina and the water content in the slurry. The pores orient along the cooling direction [25]. Porous, hollow ceramic components have also been produced by a freeze casting technique [26].

The bi-electrode supported cell (BSC) is fabricated using the FTC process. The BSC structure uses porous YSZ scaffolds on either side of a 10–20 µm electrolyte layer. The cell is structurally symmetrical as shown in Figure 7. The porous support structures can be

hierarchically graded with this process and can be tailored to maximize fuel and air flow towards the electrolyte. Both electrodes support the thin electrolyte and contain micro-channels for gas flow [27].

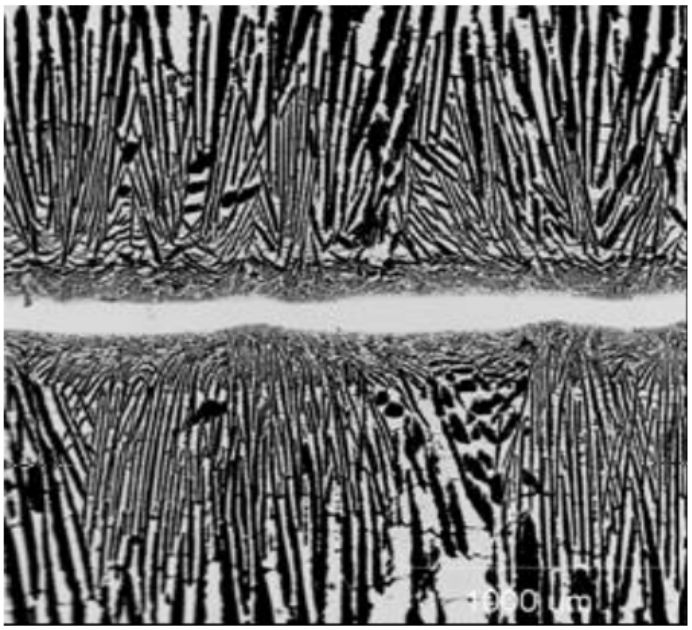

Figure 7 Cross section of sintered BSC [27]

2.6.2 Tape Calendaring

In a tape calendaring process, two or more strips of films are rolled to create multilayer structures as seen in Figure 8 [28]. The multilayer structure can be of the same film type or of different types. The process has been used to produce multilayer tapes by laminating and rolling individual layers. The multilayer tapes are cut to sizes and are then sintered to form multilayer cells. This process is also widely used in making SOFC structures.

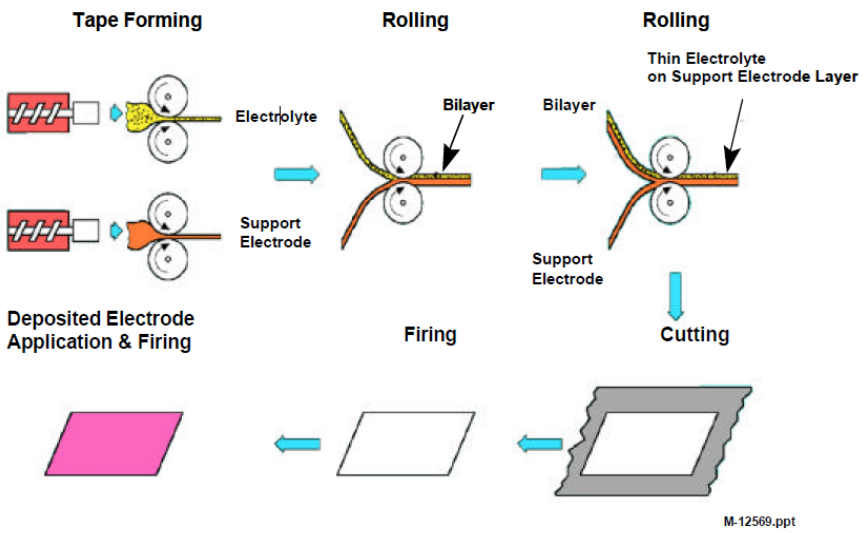

Figure 8 Tape Calendaring Process [28]

2.6.3 Screen Printing

Screen printing is a process where ink is applied to the substrate by first placing a screen over the substrate as shown in Figure 9. Ink is placed on the screen, and pressure is applied to squeeze ink through the open areas of the screen. Regions in the screen can be selectively masked off if desired. This forms an ink image on the printing substrate. This approach is also widely used in SOFC fabrication [29][30].

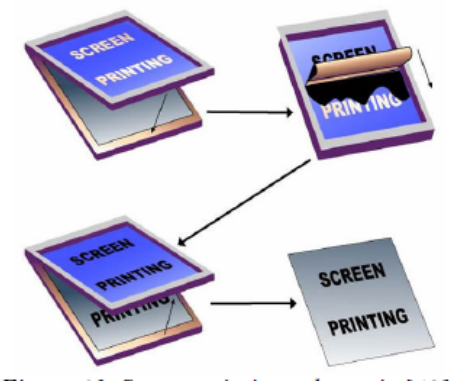

Figure 9 Screen Printing Process [31]

Active anode layers have been screen printed onto the anode substrate [29]. Similarly, screen-printing technology has been used to manufacture planar SOFC devices using YSZ as the electrolyte, LSM as the cathode and NiO-YSZ cermet for the anode. An electrode thickness of 20μm was achieved when screen printed onto the die pressed electrolyte [30].

2.6.4 Wet Spraying

The wet spraying process (Figure 10) is used for deposition of a solvent-particulate. The mixture is sprayed through a nozzle onto the substrate from a fixed distance. Wet spray processing costs much less than vacuum based CVD and sputtering deposition processing.

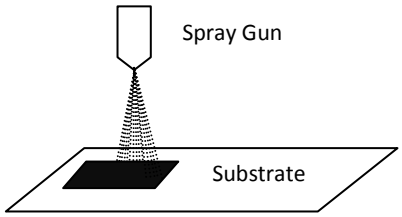

Figure 10 Wet Spraying Process

The spray coating technique has been used to fabricate dense YSZ electrolyte films on NiO–YSZ porous anode substrates. A single fuel cell of Ni–YSZ/YSZ/LSM–YSZ has been successfully prepared by this technique [32].

2.6.5 Spin Coating

Spin coating is widely used to apply thin films on a flat substrate. Spin coating uses centrifugal force that causes the fluid to spread outward radially from the center of the spinning substrate. The process involves deposition of small amount of liquid material onto the center of the substrate, which is then followed by spinning the substrate at very high speed for a fixed amount of time. The sample is then dried. The process can be repeated several times to form a multi-layered structure.

Spin coating has been used to fabricate porous cathode and thin electrolyte layers [33]. Nano structured porous thin cathodes consisting of $Sm_{0.5}Sr_{0.5}CoO_3$ (SSC) and $Ce_{0.8}Sm_{0.2}O_{1.9}$ (SDC) have been fabricated on an anode-supported electrolyte film using the spin-coating technique. The spin coated layer thicknesses were 20 μm for the SSC–SDC cathode and 25 μm for the SDC electrolyte.

2.6.6 Spray Pyrolysis

Spray pyrolysis is a process in which a thin film is deposited by spraying solution on a hot surface as shown in Figure 11. The solvent evaporates leaving solid behind on the substrate. The system contains a spray nozzle, a furnace for heating the substrate, a mechanical system for the rotor, a thermocouple included temperature controller, and an air compressor [34].

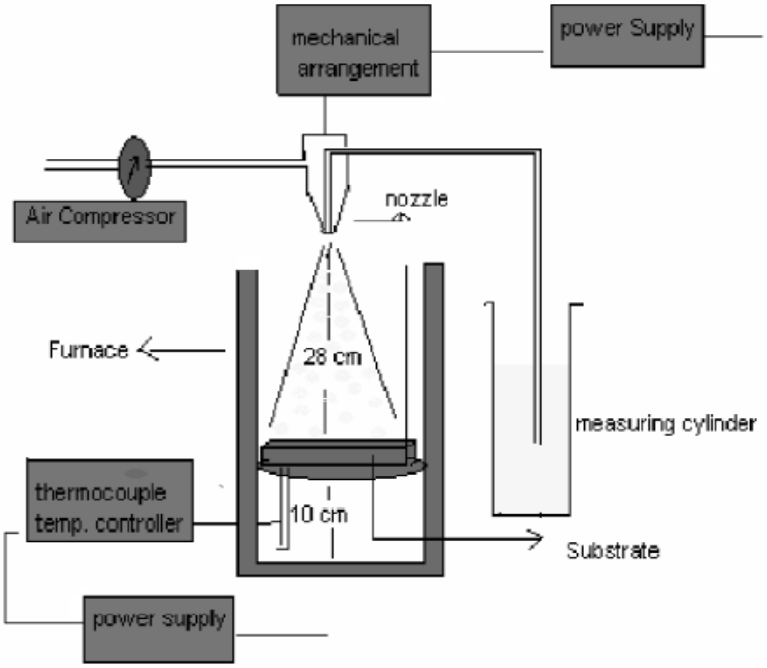

Figure 11 Schematic of Spray Pyrolysis Process [34]

The cermet SOFC anodes composed of a Ni-SDC (Nickel-Samarium Doped Ceria) SOFC have been prepared by spray pyrolysis [35].

2.6.7 Vacuum Deposition Techniques

Vacuum deposition techniques based on magnetron sputtering, vacuum plasma methods, laser ablation, and electrochemical vapor deposition can be used to fabricate SOFC structures. Below is the summary of the findings [36].

Techniques	Precursor materials	Deposition Rate	Typical microstructures	Features
RF and reactive DC magnetron sputtering	Oxide or metal target	<~5µm/h	Dense or porous films, often obtain columnar structures	Produces dense, crack-free films on dense and porous substrates; applicable to wide range of compositions; low substrate temperature; can be combined with photolithography to produce unusual configuration
Vacuum plasma spray	Oxide or metal powder feed; variation (LAFAD) used metal target	<~10µm/h	Dense or porous films; anisotropic grain structure; LAFAD method can produce multilayer, superlattice structures	Large scale deposition possible; substrates may be dense or porous; relatively high substrate temperatures
Laser ablation	Oxide or metal target	Upto 600 µm/h, most studies used 1 µm/h rate	Dense films, used to produce epitaxial films	Intermediate substrate temperatures; not easily up-scaled; particularly useful in producing high-quality oriented films for fundamental research; can be combined with photolithography to produce unusual configuration
Electrochemical vapor deposition	Metal halides ($XrCl_4$,YCL_3)	< 50µm/h	Dense films on porous substrate, columnar structures	Currently used in commercial SOFC production of thin electrolytes; high reaction temperatures; limited range of compositions possible; produces dense film on porous substrate

Figure 12 Comparison of Vacuum deposition methods for producing think films relevant to SOFC applications [36]

2.6.8 Dip Coating

Dip coating (Figure 13) is a process of creating thin films where the substrate is dipped into a liquid coating solution. The substrate is then withdrawn at a controlled speed. The thickness is influenced by withdrawal speed, fluid viscosity and the surface tension.

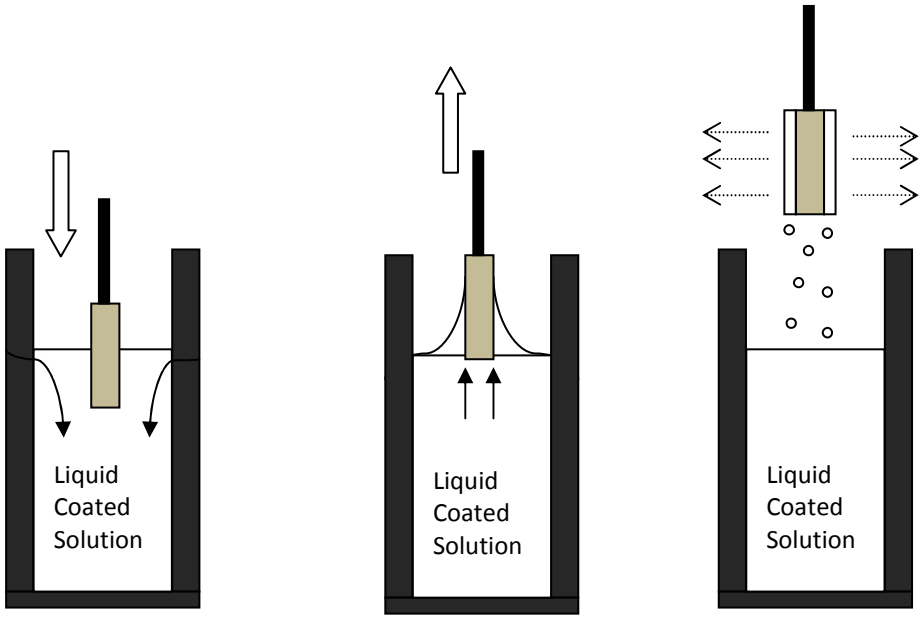

a) Dipping b) Wet Layer Formation c) Solvent Evaporation

Figure 13 Dip Coating Process

SOFC structures have been fabricated using this process. A dip-coating step followed by co-sintering has been used to form the thin and dense YSZ electrolyte films on the outer surfaces of NiO/YSZ micro tubes to form anode/electrolyte half cells. A layer of porous LSM membrane with a 20 μm thickness has also been also dip coated to form a cathode [37] [38].

2.6.9 Plasma Spraying

Plasma Spraying (PS) is a thermal spraying deposition process where material deposition occurs by introducing the material to the plasma jet originating from a plasma torch. The material can be in a liquid, suspension or powder form.

The coating material that is in a powder form is carried in an inert gas stream and into the plasma jet where it is heated and propelled towards the substrate. Because of the high temperature and high thermal energy of the plasma jet, materials with high melting points can be sprayed [39].

Thermal PS processing for nano-powder production and cell fabrication of SOFC has been performed [40]. The PS process creates sufficiently high temperatures to melt all the materials fed into the plasma. This technique has been applied to directly deposit functional layers as well as nano-powders for SOFC applications. This processing technique does not require the use of organic solvents, offers easy to adjust process parameters and significant time savings in production of the cell. The cost is also reduced when compared with thick film processes that require sintering processing steps. Plasma spraying is capable of producing extremely thin layers and can make continuously graded structures by varying the deposition material and spray distance. However, the porosity range of a plasma sprayed layer is 5 to 15%, thus making it difficult to produce a fully dense electrolyte [41].

2.6.10 Direct Write Printing

Direct write printing is a form of additive manufacturing where a part is built by printing successive layers of materials one on top of the next. One form of DW printing commercialized by nScrypt is a pressure-driven micro-extrusion process where materials in the form of an ink come out through a nozzle of a certain diameter. The deposition is robotically controlled and can produce the desired shape in a planar or a conformal surface. This technology is extremely flexible with regard to the materials and the patterns that can be printed. DW printing can print micro lines, dots, three-dimensional printed structures and conformal printed structures. The process has a wide range of applications including conductors, resistors, optics, adhesives, sealants, frit, solders, encapsulants, wire bonds, underfilling, flip-chip bumping, MEMS, etc [42].

The DW micro-fabrication approach has been demonstrated for fabrication of a single chamber SOFC [43][44]. NiO–YSZ anodes and LSM cathodes have been printed via direct write printing on a YSZ electrolyte [43].

2.6.11 Ink Jet Printing

Ink Jet printing is a variation of direct write printing where deposition occurs by dispensing droplets of ink onto the substrate through a nozzle. There are two ways of inkjet printing: thermal and piezoelectric.

Ink-jet printing has been successfully used to fabricate the electrolyte and the anode functional layers of a SOFC. The ink-jetted electrolyte layers were largely or completely free of pinholes and relatively thin in comparison to those electrolytes produced by more conventional ceramic processing methods. Ink-jetting could be used to produce the anode, electrolyte and cathode structures of a SOFC [45][46]. SOFC's have been fabricated by depositing the NiO-YSZ anode interlayer, the YSZ electrolyte layer, and the LSM-YSZ and LSM cathode layers on a NiO–YSZ support using inkjet printing. Inkjet printed SOFC's resulted in an electrochemical performance consistent with traditional processing methodologies [47].

2.6.12 Comparison of Popular SOFC Fabrication Processes

Table 7 summarizes the more common SOFC fabrication techniques along with some characteristics [31]. It is challenging to develop novel methods which can precisely control the pore structure (e.g., porosity, pore size and shape, interconnection between pores, and pore alignment) in a cost effective way to improve mechanical properties and electrical performance of a SOFC. Of all the processes, the freeze tape casting process used to produce the bi-electrode supported cell (BSC) is one of the most promising methods for the production of porous electrodes [27]. Table 8 provides a summary of some of the major manufacturers of SOFC's and their respective technologies [48][49].

Table 7 Summary of SOFC fabrication processes [31]

Fabrication Technique	Grading capability	Cost (time/complexity)	Porosity	Thickness
Tape casting	Poor	High	0-60	>7 µm
Screen printing	Poor	High	0-60	>8 µm
Dip coating	Poor	High	0-60	>10 µm
Spin coating	Yes	High	0-60	>1 µm
Extrusion casting	No	Low	0-60	N/A
Tape calendaring	Poor	Low	N/A	N/A
Plasma spray	Yes	Low	5-20	>Particle size
Electrostatic spray deposition	Yes	High	0-60	>Particle size
Ultrasonic mist spray pyrolysis	Yes	Medium	0-55	>Particle size

Table 8 SECA Industry Team Design & Manufacturing [48][49]

SECA Industry Team Design & Manufacturing		
Team	**Design**	**Manufacturing**
FuelCell Energy Versa Power Systems WorleyParsons PNNL	▸ Anode-supported planar ▸ < 800° C ▸ Low-cost ferritic SS interconnects ▸ 550cm^2 active area cells	▸ Tape casting ▸ Screen printing ▸ Stamped interconnects
UTC Power Delphi Battelle Memorial Institute	▸ Anode-supported planar ▸ < 800° C ▸ Low-cost ferritic SS interconnects ▸ 403 cm^2 active area cells ▸ Ultra-compact ▸ Rapid transient capability	▸ Tape casting ▸ Screen printing ▸ Stamped interconnects ▸ Laser welding
Rolls-Royce Fuel Cell Systems Case Western Reserve University University of Connecticut ORNL PNNL	▸ Integrated planar (segmented-in-series) ▸ < 900° C ▸ Pressurized operation	▸ Extrusion ▸ Screen printing

2.6.13 Future State of SOFC's

The Solid State Energy Conversion Alliance (SECA) was founded in the fall of 1999. SECA is collaboration between the Federal Government, private industry, academic institutions and national laboratories devoted to the development of low-cost, modular and fuel-flexible SOFC technologies suitable for a variety of power generation applications [48][49].

The SECA FY 2010 annual report emphasized that the SECA fuel cell program is a critical element of the Department of Energy's (DOE) office of fossil energy technology portfolio. Currently, coal is a primary resource for reducing dependence on imported oil and natural gas. In the US, more than half of the nation's electricity supply is generated from coal. Coal is a nonrenewable energy source that produces sulfur dioxide (SO_2), nitrogen oxides (NO_x), carbon dioxide (CO_2) and particulates. SO_2 has been linked to acid rain and increased incidence of respiratory illnesses. NO_x has been linked to the formation of acid rain and photochemical smog. CO_2 is the primary greenhouse gas emission from energy use. Particulates have been linked to the formation of acid rain and increased incidence of respiratory illnesses [48][49].

There is a need to develop an alternative energy source that is clean, climate friendly and would reduce dependence on imported oil. SECA's technology offers greater than 99 percent carbon capture, less than 0.5 parts per million (ppm) NO_x emissions, reduced water requirements, and a coal-to-electricity efficiency exceeding 50 percent on a higher heating value (HHV) basis and as high as 60 percent HHV for advanced pressurized systems (Figure 14) [49][50].

The ultimate objective is to enable the generation of efficient, cost-effective electricity from domestic coal with near-zero atmospheric missions of CO_2 and air pollutants (99% CO_2 capture) and minimal use of water in central power generation applications.

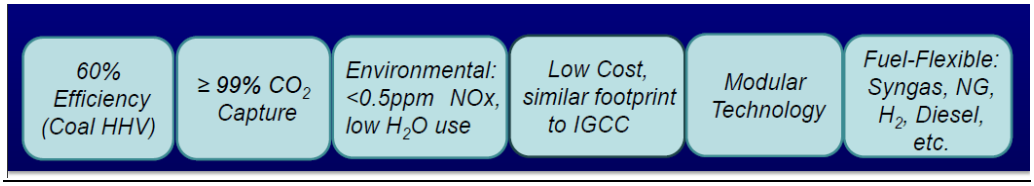

Figure 14 SECA Objectives [49]

The SECA program is focused on developing technology required for competitive SOFC stack technologies that can be mass-customized for a wide range of applications, such as stationary power generation, mobile power generation, military power applications, transportation applications, etc. The objectives of the SECA program (Table 9) in the year 2007 were as follows:

Table 9 SECA Objectives

Current SOFC Characteristics	SECA Objectives
High operating temperature	Wider operating temperature range
Intolerant of sulfur in fuels	Sulfur-tolerant anode
Internal or external fuel reformation	Capability for on-cell reformation
Reliance on natural gas or other limited fuels	Viable fuel processors for common liquid fuels (diesel, kerosene)
Limited thermal cycling, load follow capability	Improved capabilities
Low system power density	Higher power density cells, parts and weight reduction

Future SECA program objectives include:

- By 2010, a test stack running for 5,000 hours with a degradation of less than 2.0 percent per 1,000 hours and costs of $700 per kilowatt or less for the system power block. The SECA cost goal for stacks is $175 per kilowatt or less.
- By 2012, a 250-kilowatt to 1-megawatt fuel cell module demonstration.
- By 2015, a 5-megawatt proof-of-concept fuel cell system to demonstrate system integration, heat recovery turbines, and power electronics.
- By 2020, a full-scale demonstration of a 250- to 500-megawatt integrated gasification fuel cell power plant.

The high efficiency and environmental friendliness of SOFC's have already been well established by Siemens Energy for stationary base-load applications. Product validation and cost reduction are now primary objectives for stationary market applications, with further cost and performance improvements needed for other mass market applications, such as military and transportation. Under Siemens Energy's SECA program, the above objectives are being addressed with the expectation that small-scale SOFC products can be started quickly, cycled in and out of operation as needed, and operated. Below is a list (Table 10) of some of SOFC manufacturers and their technologies [48].

Table 10 SOFC Manufacturers and their Technologies [48]

Manufacturer	Country	Achieved	Year	Attributes and status
Acumentrics Corp.	USA	2 kW	2002	Microtubular SOFCs, 2kW for uninterruptible power
Adelan	UK	200 W	1997	Microtubular, rapid start-up and cyclable
Ceramic Fuel Cells Ltd	Australia	5 kW 25 kW	1998 2000	Planar SOFC, laboratory stack testing, 600 operating hours for 5 kW stack, developing 40 kW fuel cell system
Delphi/Battelle	USA	5 kW	2001	Developing 5 kW units based on planar cells
Fuel Cell Technologies (with Siemens Westinghouse Power Corporation)	Canada	5 kW 2 kW	2002 2002	5 kW prototype SOFC under test, 40 percent electrical efficiency. Several Field trails planned in Sweden, USA, Japan, etc.
General Electric Power Systems (formerly Honeywell and Allied Signal)	USA	0.7 kW 1 kW	1999 2001	Planar SOFCs, atmospheric and hybrid systems
Global Thermoelectric	Canada	1 kW	2000	Planar SOFCs, 5000 hours fuel cell test
MHI/Chubu Electric	Japan	4 kW 15 kW	1997 2001	Planar SOFC, laboratory stack testing, 7500 operating hours
MHI/Electric Power Development Co.	Japan	10 kW	2001	Tubular SOFC, pressurized operation, 10 kW laboratory testing for 700 hours
Rolls-Royce	UK	1 kW	2000	Planar SOFC, laboratory testing, developing 20 kW stack for hybrid systems
Siemens Westinghouse Power Corporation	USA	25 kW 110 kW 220 kW	1995 1998 2000	Tubular SOFC, several units demonstrated on customer sites. More than 16,000 single stack operating hours, first hybrid SOFC demonstration
SOFCo (McDermott Technologies and Cummins Power Generation	USA	0.7 kW	2000	Planar SOFC, laboratory testing, 1000 operating hours, developing 10 kW versatile SOFC unit
Sulzer Hexis	Switzerland	1 kW	1998-2002	Planar SOFC, field trails of many testing
Tokyo Gas	Japan	1.7 kW	1998	Planar design, laboratory testing
TOTO/Kyushu Electric Power/Nippon Steel	Japan	2.5 kW	2000	Tubular SOFC, laboratory testing, developing 10 kW system for 2005

2.7 PROBLEM STATEMENT

SOFC's consist entirely of solid-state materials and utilize a fast oxygen ion conducting ceramic as the electrolyte; SOFC's operate in the temperature range of 700–1000°C. SOFC's can produce electrical energy for as long as the fuel and oxidants are supplied to the electrodes. The performance is expected for at least 40,000 hours. However, the performance of SOFC's degrade over time, which limits the practical operating life of SOFC's as indicated in Figure 15. The aging mechanisms of the anode, cathode, and interconnects have been explored in many studies [9][16][51]. Some literature suggests that development of new materials, optimization of microstructures and lower operating temperatures are desirable for the long-term stability of SOFC's [51][52].

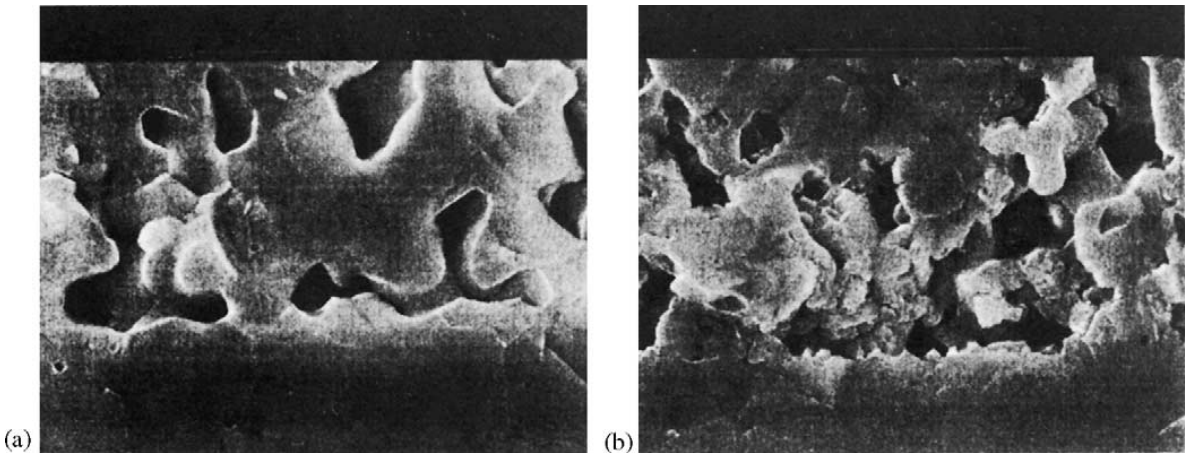

Figure 15 Structural stability in the composite cathode during operation at 850 ◦C, 300mAcm−2 in air: (a) Initial state and (b) after operation of 5000 h [51]

The high-temperature operation of SOFC's places rigorous durability requirements on all SOFC components. A key challenge for SOFC technology is the development of low-cost materials with high durability at high temperatures.

The fabrication of ceramic structures is a technical challenge for SOFC's. The state-of-the-art processing methods for the fabrication of SOFC single cells is layer-by-layer deposition methods such as tape casting, screen printing, wet spraying and tape calendaring. These steps are then followed by co-sintering. However, these traditional wet ceramic techniques face certain problems [41]:

- Multiple separate instruments such as an extruder or tape caster, screen-printer, and furnaces, etc. are needed for the multiple steps.
- High-temperature firing leads to a substantial and rapid increase in capital costs due to the long processing times. The time required to ramp the deposited layers to and from a high-sintering temperature and hold them there for sufficient densification times is significant.
- The size enlargement of single cells creates serious problems due to large total shrinkage or thermal expansion mismatch strain, which leads to macro-cracks, severe warping, or cell fracture during high temperature firing steps.

- High-temperature firing steps lead to inter-reactions between adjacent cell layers.
- Some novel anode materials cannot be sintered at high temperatures due to low melting temperatures.

Plasma spray (PS) processing is an alternative method for fabricating SOFC's. PS processing potentially provides a much simplified and cost-effective choice for fabricating SOFC components [53]. This process allows one to make a SOFC by spraying the entire multilayer SOFC in one consecutive plasma process, using only one piece of equipment and within a few minutes. The layers are very thin, which results in improved performance and reduced material consumption. However, it is a capital-intensive technology. Furthermore, the process development work and the transfer of the technology onto an industrial scale is a challenge [54][55].

In the context of SOFC electrode structures, porous materials play an important role in the development of fuel cell technology. The function of these materials includes the transport of gases to and from the active sites, the mechanical support of the structure, and the support of active electrodes. Understanding of the key parameters influences the performance of these materials in an operating SOFC. It remains a challenge facing the fuel cell technology, and is an area where there remain significant opportunities for research [3].

It has been shown that increasing levels of graded porosity improves the electrode performance [56][57][58][59]. The grading of electrodes reduces the mass transfer losses and increases the volumetric reactive surface area close to the electrode-electrolyte interface. However, the highly graded structures produced are complex, and hence are more costly to fabricate. Also, the sintering temperature and fabrication techniques have effects on the microstructures of the graded electrodes and therefore on their electrochemical performance.

It is challenging to develop novel methods which can precisely control the pore structure (e.g., porosity, pore size and shape, interconnection between pores, and pore alignment) and hence the porosity of a structure. The conventional methods are not well-suited for precise local control of material and/or structure. Thus, there is a need for an alternative fabrication method.

Today, an increasingly popular method for fabricating SOFC is freeze tape casting, which works well for a simple part such as a multilayer structure. However, it faces challenges when it comes to fabricating multifunctional, multimaterial components with complex geometries. Generally, the resulting microstructure using freeze tape casting is controllable, but the linear channels can result in shrinkage and curling along that one axis. The structure is mechanically strong in only one direction. The aim is to develop alternative methods that allow channels in any orientation in order to produce balanced shrinkage stresses with strong mechanical strength in all direction. It must also be capable of fabricating multifunctional, multimaterial components with complex geometries.

One such approach is to employ direct-write printing methods to allow the structure to be engineered. It is an additive manufacturing process, where material deposition and path control can occur simultaneously. The fuel cell material is introduced as a paste, which is typically composed of the electrode material, an ink vehicle, a fugitive material and some additives. The pores are defined by the holes left by fugitive material that burns off at sintering temperatures. By varying the amount and size of fugitive material, various pore morphologies can be obtained.

This process allows the flexibility of changing the ink composition within a layer, unlike other processes that can only change composition in between layers. The advantages, disadvantages and limitations of direct write methods will also be discussed.

A graded electrode structure printed via 3D direct-write printing will be demonstrated. The structures can be stacked to form a multi-layer component using this method. For instance, by changing the composition of the layer from layer-to-layer (non-porous to porous or vice-versa), a hierarchically graded porous structure can be engineered.

Anode-supported planar button cells and cathode-supported planar button cells will be fabricated using 3D direct write printing methods thereby demonstrating the process capability of producing anode and cathode layers via 3D direct write printing.

Last, various engineered electrode structures will be demonstrated. An alternative method of creating the electrode structure similar to that of a bi-electrode supported cell (BSC) using 3D direct write printing will be presented. Single cell BSC's have already been demonstrated; however, the fabrication and performance of a multi-cell stack still remains a challenge. 3D direct write methods could potentially be used to resolve this issue of fabricating the multi-cell BSC stack. Geometries that are not possible by any other methods will also be discussed.

CHAPTER 3: METHODOLOGIES

3.1 LOCAL CONTROL OF ELECTRODE ARCHITECTURES

The first problem to be approached addresses the desire to hierarchically grade the porosity of the electrodes, i.e. create smallest pores on the electrode structure in the Triple Phase Boundary (TPB) region (electrode/electrolyte interface), and make the largest pores at the electrode/fuel (or air) interface. The structure in between should be graded. The TPB is a conceptual zone in the cell where the hydrogen oxidation reaction and the oxygen reduction reaction occurs. It is highly desirable to increase the TPB zone. The synthesis approach being explored involves direct-write printing in which the fuel cell paste is micro-extruded onto the substrate, one layer at a time.

Pores are defined in the structure by introducing pore formers, such as graphite powder, to the fuel cell ink in the desired proportion. During the sintering process the graphite powder burns off, leaving behind pores which make the structure porous. By varying the pore former concentration in the paste, a more or less porous structure can be fabricated. In theory, the higher the concentration of pore formers, the more porous the structure is. Using this concept, hierarchically graded porous structure can be fabricated. By controlling the concentration of pore formers in the paste for each individual layer being printed or even within a given layer, the porosity of a structure can be locally controlled. An nScrypt Smartpump micro-extrusion system is used for this purpose. This method allows printing of layers as thin as 10 µm and line widths as narrow as 110 µm (based on post sintered NiO-YSZ ink profiles on a YSZ substrate). This process allows the ink composition to be changed within a layer as well as in-between layers.

The second problem to be approached involves engineering a bi-electrode supported cell (BSC) like structure by printing ribs separated by channels via direct write methods. The goal is

to create ribs with vertical walls having extremely low tortuosity (discussed in section 3.6). Tortuosity is a defined as a ratio of the length of the path the gas takes to reach point A to point B to the shortest distance between points A and B. This approach:

- Allows reactant gases to easily permeate the electrode
- Provides a shorter conductive path for electrons and ions, thus reducing overall ohmic losses
- Creates a surface that is easier to infiltrate with active cathode materials
- Opens up the possibility of creating arbitrarily complex rib/channel architectures designed to balance shrinkage stresses during sintering, thus improving mechanical strength and durability of the cell.

Arbitrarily tall ribs can be achieved by printing lines on top of each other. Using this approach, electrode geometries similar to those of the BSC architecture can be created. A baseline model will be presented that will allow tailoring the features of the lines printed, such as line width, line height, line profile, channel width, etc., to get a desired geometric shape.

All fabrication work, unless otherwise specified, has been done via direct-write printing using an nScrypt Tabletop Series Smartpump micro-extruder. The various tools used throughout this research were:

- nScrypt Tabletop Series Smartpump micro-extruder
- THINKY mixer – ARM 310
- MTI Furnace – KSL1600X
- Hirox Microscope – KH-7700
- 45 TON SHOP PRESS
- Scanning Electron Microscope (Amray 1830 SEM)
- GE 250W heat lamp

- A set of 15mm pressing dies from MTI Corporation – EQ-Die-15D

3.2 GENERAL CHARACTERIZATION OF DIRECT-WRITE PRINTED STRUCTURES

Although there are different direct write printing technologies, nScrypt's micro-extrusion DW process is used in this research. nScrypt's process functions in a similar manner to how one would write using a pen or pencil. The material being printed is a particulate loaded ink or paste. Fabrication is carried out by laying down lines in any direction desired using a 3-axis computer controlled tool-path, so any geometry can be printed on a flat or a conformal surface (i.e. surface that conforms to the shape of a part). The tool path is fed in the form of machine code for the system's Aerotech motion controller. The printed lines have certain width, height and profile whose values are a function of the selected process parameters.

Suppose that one would like to print a solid 1 mm X 1 mm square. If the line width is 0.2mm, then 5 lines of 1mm length could be printed to make a square. However, the extruded bead of ink/paste produces a rounded line as shown in Figure 16, so a suitable step-over distance must be selected to create a flat surface. Step-over is the distance one tool scan is offset from the adjacent scan, just like in CNC machining. Figure 17 shows a profile of lines printed at different step-over distances. If a step-over of 0.1mm is chosen in the above example, then a total of 10 lines of 1mm length will be needed to make a 1mm X 1mm square. In general, the line profile (tapered angle, line width and height) and step-over needed must be experimentally determined each time a new ink or paste is formulated.

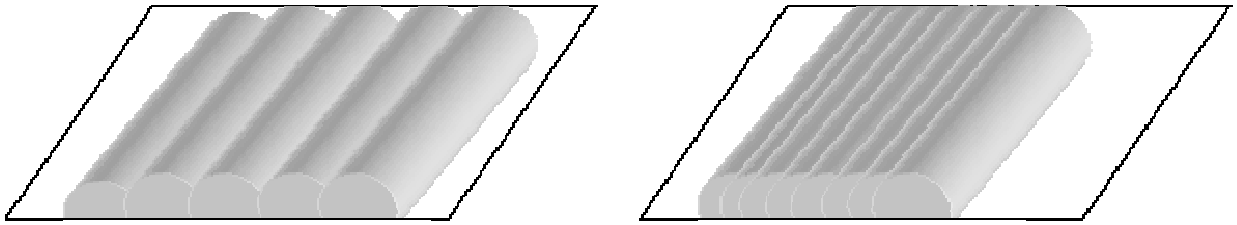

a) Line printed at a different step-over produces different surface profile

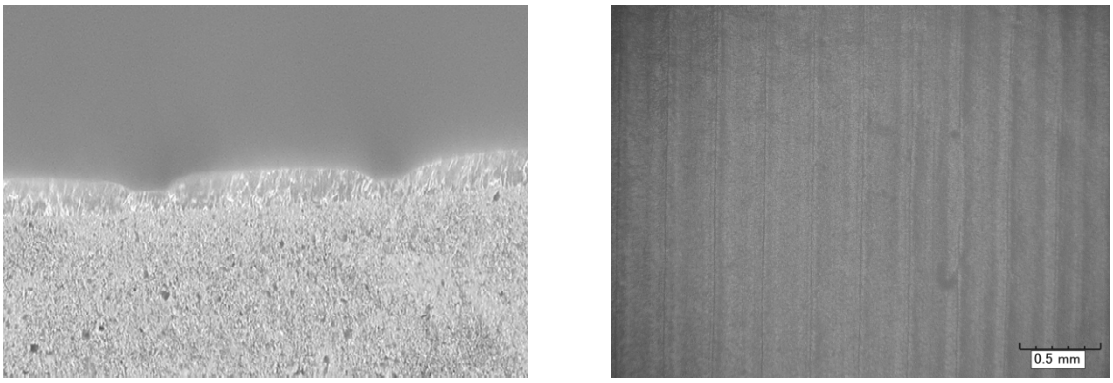

b) Track marks on a printed profile: a) Side-view (left) b) Top-down view (right)

Figure 16 Track marks left after printing a) Simulated profile b) Actual Profile

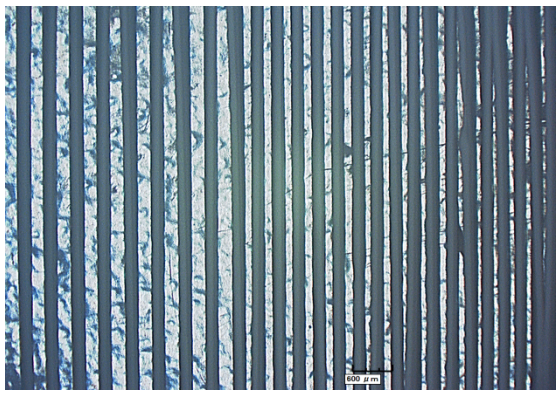

Figure 17 Array of printed lines with varying step-over (top-down view)

The characteristics of the ink need to be understood as well. The use of highly viscous inks typically results in printed tracks with fairly vertical side walls, whereas the use of less viscous inks typically results in printed tracks with a more tapered shape as shown in Figure 18. The

surface tension of the substrate also plays a vital role, as it exerts external force on the deposited ink.

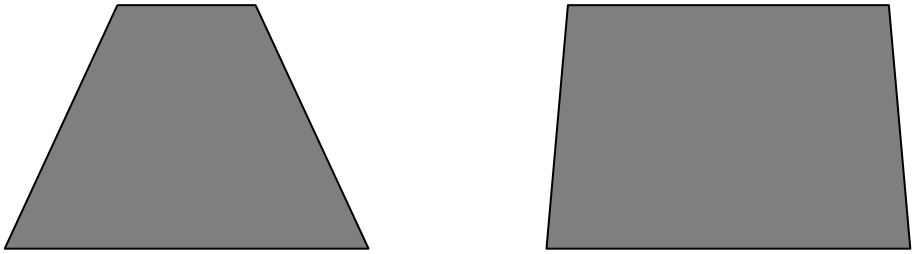

Figure 18 Profiles Printed tapered profile of less viscous ink (left) vs. high viscous ink (right)

The printing is also heavily dependent on the nScrypt tool's process parameters. The controllable tool process parameters of an nScrypt Smartpump are:

a) Translation Speed (mm/sec) – The printing speed in x-direction (f_x) and y-direction (f_y).
b) Valve Open Position (mm) – The distance the valve opens to control the flow of ink
c) Dispensing height (mm) – The distance between the tip of the nozzle and the substrate
d) Pressure (PSI) – The amount of air pressure applied to syringe containing the ink or paste being dispensed.

Additional factors the user has control over include:

i. Nozzle size – The diameter of the orifice in the dispensing tip
ii. Ink formulation - Particle size, solid loading fraction, viscosity, etc.
iii. Post deposition sintering schedule – Ramp up rate, hold temperature, hold duration

To summarize, the printing output is heavily dependent on a significant number of process parameters and additional factors under the user's control.

3.2.1 Preliminary Process Characterization

A preliminary study was conducted to examine the effect of *Speed*, *Pressure*, and *Valve Position* on the line width and line height. Figure 19 shows the tool configuration.

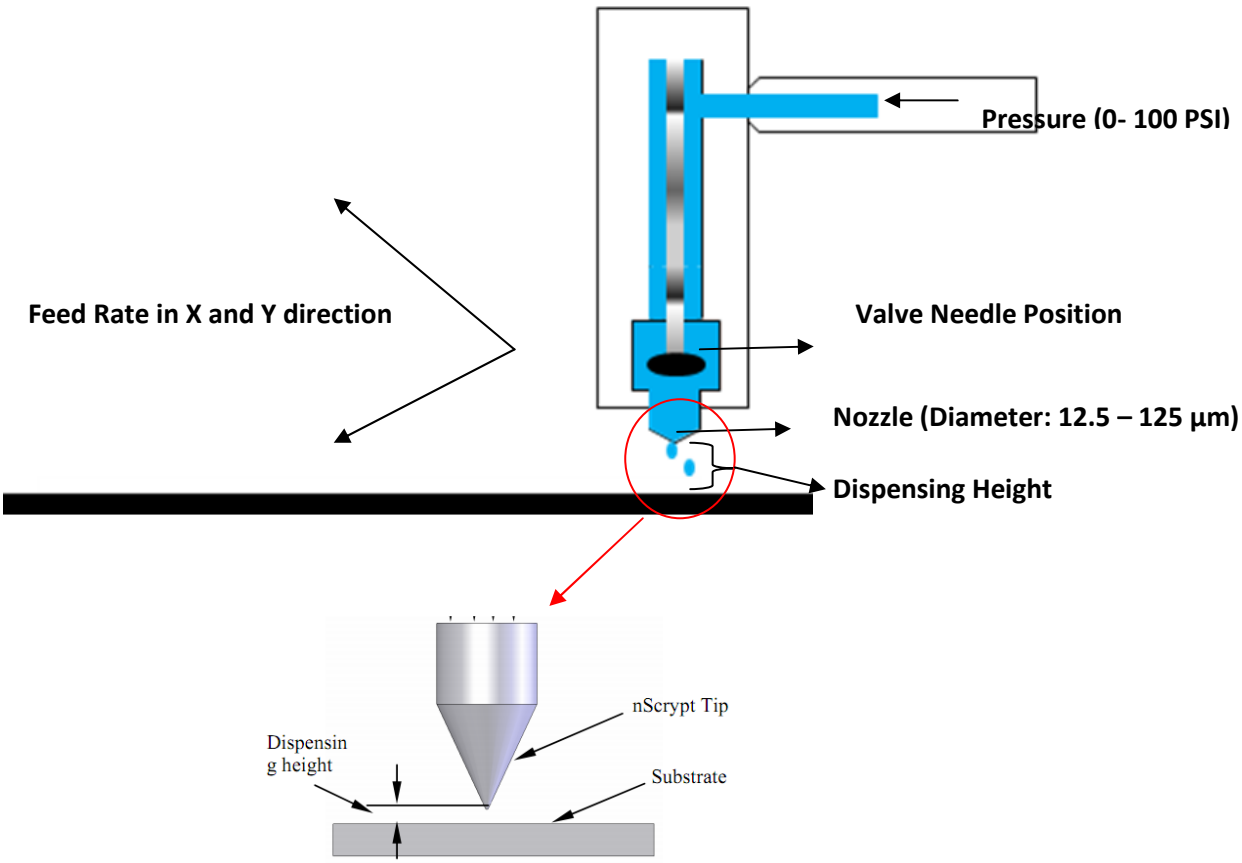

Figure 19 Schematics of a Smartpump

Lines were printed using the process settings shown in Table 11, and the resulting line widths and heights were measured using a Hirox KH-7700 optical microscope. The NiO-YSZ ink printed was prepared by mixing 8.5 grams NiO-YSZ (Fuel Cell Materials) with 4ml Terpineol in a Thinky ARM 310 mixer at 2000 rev/min for 10 minutes. This ink was printed on mylar film through a 280 µm ceramic nozzle on the nScrypt machine with a dispensing height of approximately 100 µm. The samples were dried under a heat lamp for one hour.

Table 11 General Linear Model: Height, Width versus Speed, Pressure, Valve Position

Factor	Type	Levels	Values
Speed	Fixed	8	5, 10, 15, 20, 25, 30, 35, 40 mm/sec
Pressure	Fixed	3	0.4, 0.5, 0.6 V (0.5V = 10PSI)
Valve Position	Fixed	3	0.5, 0.6, 0.7 mm

One line was printed at each setting. Table 12 and Table 13 show line width and line height results from the preliminary tests respectively.

Table 12 Line width results

	Pressure	0.4	0.4	0.4	0.5	0.5	0.5	0.6	0.6	0.6
	Valve Position	0.5	0.6	0.7	0.5	0.6	0.7	0.5	0.6	0.7
Speed										
5		830	836	930	1338	1394	1400	2159	2237	2413
10		600	650	708	1028	1018	1013	1508	1585	1600
15		516	588	640	904	914	904	1307	1431	1460
20		454	521	558	816	831	821	1131	1177	1178
25		413	480	511	764	728	754	1017	1074	1105
30		366	433	486	692	723	692	914	986	950
35		341	418	424	619	645	666	898	966	865
40		320	392	393	578	599	568	826	852	865

Table 13 Line height results

	Pressure	0.4	0.4	0.4	0.5	0.5	0.5	0.6	0.6	0.6
	Valve Position	0.5	0.6	0.7	0.5	0.6	0.7	0.5	0.6	0.7
Speed										
5		57	57	59	95	101	109	137	138	184
10		37	54	43	63	73	83	80	76	102
15		30	40	39	60	62	62	74	77	85
20		28	39	33	45	50	52	66	75	78
25		28	32	28	48	45	48	55	63	81
30		25	33	32	37	40	47	52	60	71
35		17	31	26	35	39	44	45	95	71

The data was entered into JMP for statistical evaluation. The ANOVA results for the line height suggest that Speed, Pressure, Valve Position, and the interaction between Pressure*Valve Position and Pressure*Speed are statistically significant factors (α=0.05). The ANOVA results for the line width were the same as the ones for line height. Also, the line height and width were

highly correlated (R = 0.92), so it may not be necessary to measure both features for characterization purposes provided similar inks are used (Figure 20 (c)).

Table 14 shows the analysis of variance (ANOVA) results for printed line heights and Table 15 shows the ANOVA results for printed line widths.

The ANOVA results for the line height suggest that Speed, Pressure, Valve Position, and the interaction between Pressure*Valve Position and Pressure*Speed are statistically significant factors (α=0.05). The ANOVA results for the line width were the same as the ones for line height. Also, the line height and width were highly correlated (R = 0.92), so it may not be necessary to measure both features for characterization purposes provided similar inks are used (Figure 20 (c)).

Table 14 ANOVA for line height

Summary of Fit

RSquare	0.99818
RSquare Adj	0.995385
Root Mean Square Error	29.43096
Mean of Response	884.9167
Observations (or Sum Wgts)	72

Analysis of Variance

Source	DF	Sum of Squares	Mean Square	F Ratio
Model	43	13301222	309331	357.1200
Error	28	24253	866	Prob > F
C. Total	71	13325476		<.0001*

Effect Tests

Source	Nparm	DF	Sum of Squares	F Ratio	Prob > F
Pressure	2	2	2410659.7	1391.544	<.0001*
Valve Position	2	2	38053.4	21.9662	<.0001*
Speed	7	7	297569.4	49.0774	<.0001*
Pressure*Valve Position	4	4	19891.6	5.7412	0.0017*
Pressure*Speed	14	14	1070345.1	88.2647	<.0001*
Valve Position*Speed	14	14	18592.6	1.5332	0.1630

Table 15 ANOVA for line width

Summary of Fit

RSquare	0.987906
RSquare Adj	0.969332
Root Mean Square Error	5.140873
Mean of Response	56.73611
Observations (or Sum Wgts)	72

Analysis of Variance

Source	DF	Sum of Squares	Mean Square	F Ratio
Model	43	60445.986	1405.72	53.1894
Error	28	740.000	26.43	Prob > F
C. Total	71	61185.986		<.0001*

Effect Tests

Source	Nparm	DF	Sum of Squares	F Ratio	Prob > F
Pressure	2	2	9910.0750	187.4879	<.0001*
Valve Position	2	2	260.8333	4.9347	0.0146*
Speed	7	7	1545.9000	8.3562	<.0001*
Pressure*Valve Position	4	4	960.8889	9.0895	<.0001*
Pressure*Speed	14	14	4940.5833	13.3529	<.0001*
Valve Position*Speed	14	14	437.0000	1.1811	0.3409

Among all the significant factors and interactions, Pressure has the most impact on the printed profile (both line width and height) followed by interaction between Pressure*Speed and then the Speed. The effects are more visible in the box plots shown below in Figure 20. As pressure is increased the line width and the line height increases. The more open the valve is the more comes out, which increases the line width and the line height. As for speed, the faster the printing process the thinner the line width and smaller the line height.

As previously mentioned, however, the shape of the deposited line is very much dependent upon ink properties and surface tension with the substrate. Although the ANOVA showed no or very little statistical significance of other interactions, it is important to understand that the process parameters influence each other.

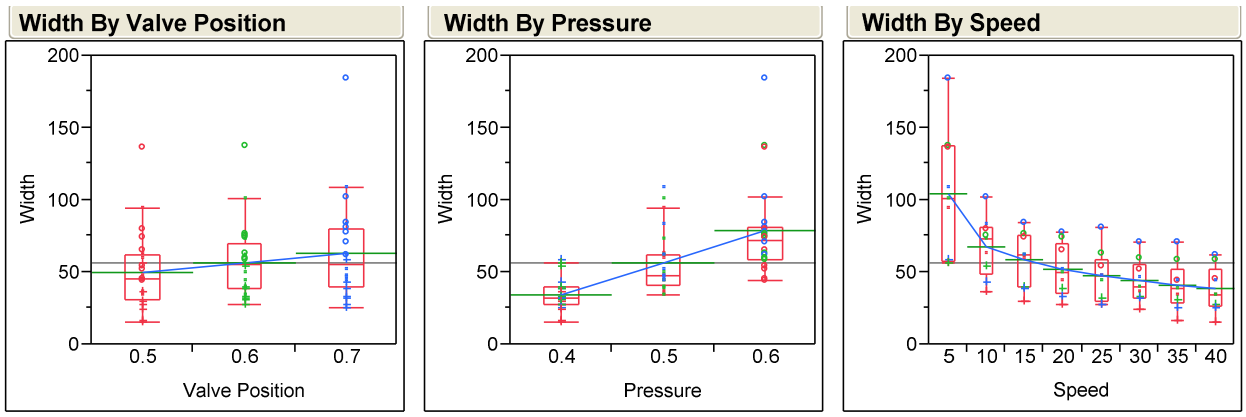

a) Box plot for Line width vs. Valve Positron , Pressure and Speed

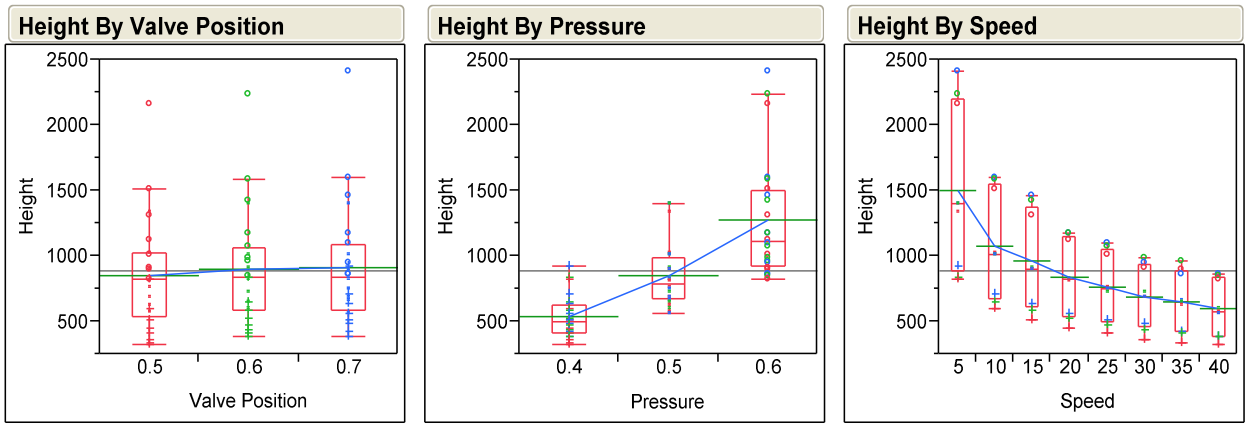

b) Box plot for Line height vs. Valve Positron , Pressure and Speed

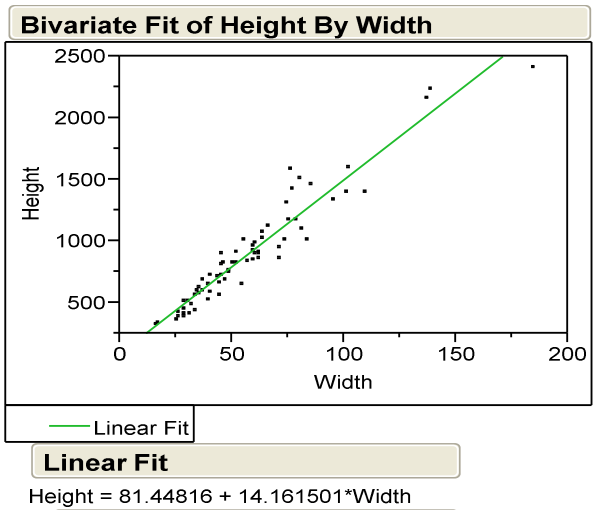

Summary of Fit	
RSquare	0.920848
RSquare Adj	0.919717
Root Mean Square Error	122.7507
Mean of Response	884.9167
Observations (or Sum Wgts)	72

c) Correlation between height and width

Figure 20 Box plots and the height/width correlation

There are limitations on how much speed, pressure, valve opening and dispensing height can be adjusted. If the valve is fully open, further opening it would not cause a significant impact on the printing output.

Increasing the pressure increases the ink flow rate, which in turn produces wider lines. Once the maximum flow out rate through the nozzle is achieved, further increases in pressure do not significantly change output. Rather, it has been observed that excessive air pressure can actually lead to air pockets in the ink which lead to voids and uneven lines during printing.

The faster the lines are printed, the narrower the lines become. However, there is a limit to how fast a given ink can successfully be printed. The upper limit depends on a number of factors, such as ink viscosity, pressure applied, nozzle diameter, etc. Assuming all other parameters are kept constant, there is a maximum speed above which the printed lines begin to break up into a series of dots rather than a continuous path (Figure 21). If the linear flow rate of ink through the nozzle is lower than the translation speed of the nozzle over the substrate, then a tensile stress is exerted on the extruded ink (i.e. the extruded bead is being “stretched” out as it exits the nozzle). If that stress is great enough, the ink stream begins to break up. Conversely, it is possible for the flow rate of ink out of the nozzle to exceed the translation speed of the nozzle over the substrate. In this case, the extruded bead can actually experience compression which leads to a barreling effect. Based on the preceding explanation, the significance of interaction effects between Pressure and Speed in the ANOVA are not surprising.

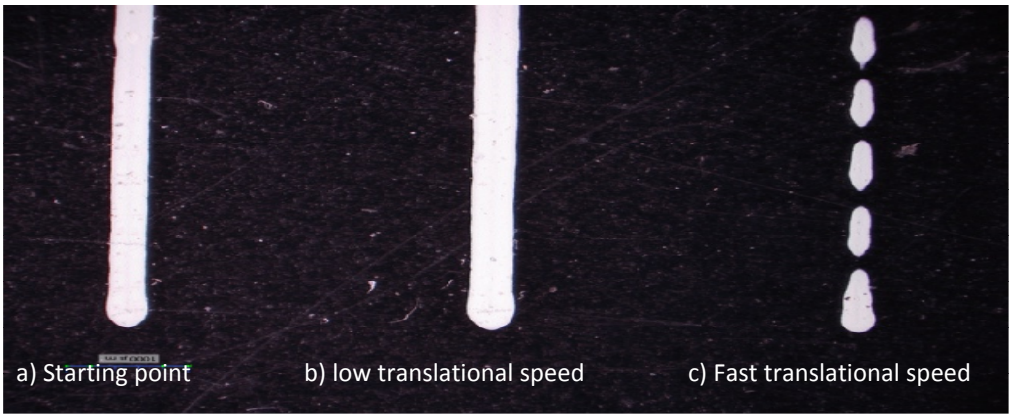

Figure 21 Effect of speed on line profile

The dispensing height is the distance between the nozzle tip and the substrate as shown in Figure 19. Li et al. [42] showed that the ink flow rate increases to a point as the dispensing height is increased (assuming pressure is kept constant) as shown in Figure 22. The smaller the dispensing height, the more it affects the flow-rate. The height can only be increased to a certain value, beyond which the ink will not dispense onto the substrate. For many instances, the ink will move up the nozzle if the dispensing height is too high because the ink is going to flow in the direction of least resistance.

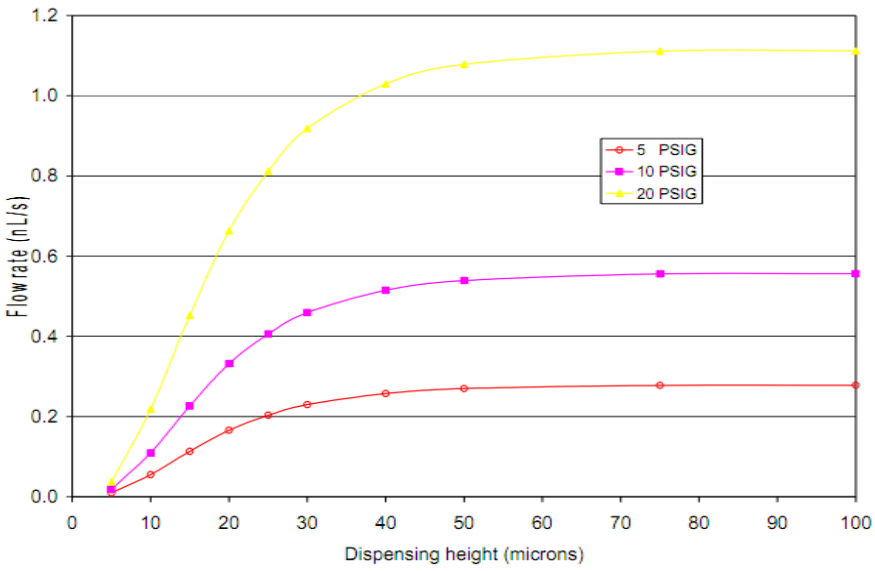

Figure 22 Flow rate vs. Dispensing height [42]

3.2.2 Effect of Ink Formulation

The ink formulation method used was the same for all DW experiments described here. The flow chart in Figure 23 shows the steps used in creation of an ink for printing purpose. Once the desired quantity of fuel cell powders, pore former, ink vehicle or any other materials was measured, mixing was done in a THINKY ARM 310 mixer (www.thinkyusa.com). This mixer utilizes counter rotating centrifugal forces to create a thoroughly mixed ink. All the ink created in this research was mixed for 10 minutes @ 2000 RPM in the THINKY mixer unless otherwise specified.

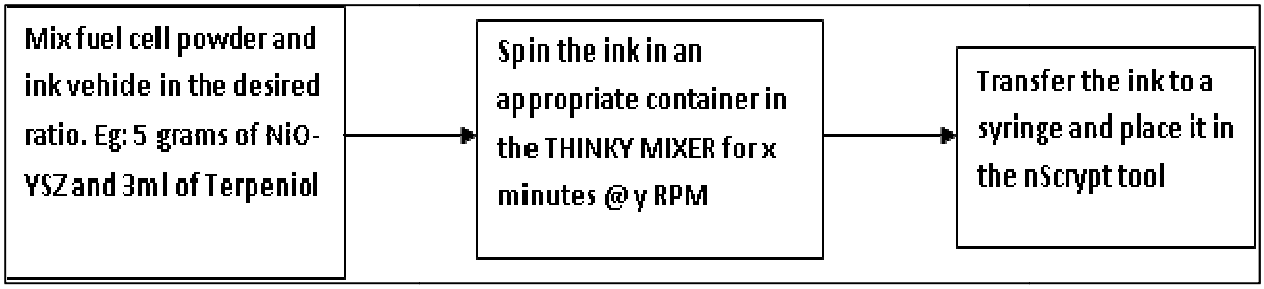

Figure 23 Ink formulation method for DW experiments

It is important to note that the type of material, the material particulate size/size distribution, and the amount of ink solvent and its type (polar or non-polar) greatly affect the ink rheology. There are two rheological classifications based on whether the ink is Newtonian or non-Newtonian. One of the most important ink properties is viscosity. Water has a viscosity of 1 centipoise (cP) and is a Newtonian fluid. Effective viscosity can be better understood by looking at the behavior of viscous fluids at different shear rates. By examining ink viscosity as a function of shear rate, one can determine whether the ink is Newtonian, thixotropic, dilatant or pseudoplastic as shown in Figure 24.

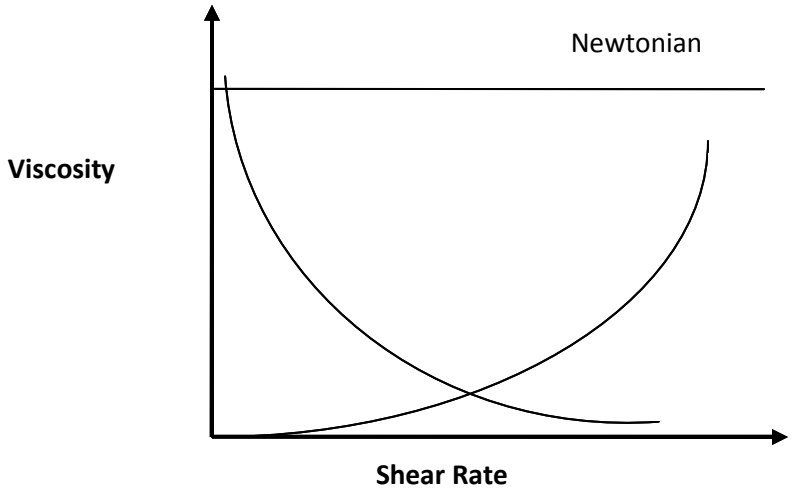

Figure 24 Viscosity vs. Shear Rate for various fluid types

Rheological behavior of the NiO-YSZ inks used in this research was measured using a Brookfield viscometer and was shown to exhibit thixotropic behavior as seen in Figure 25. A thixotrpic ink becomes less viscous when stirred. The ink constitutents were 12 grams NiO-YSZ powder (Fuel Cell Materials) and 10ml Terpeniol, mixed in a THINKY mixer for 10 minutes.

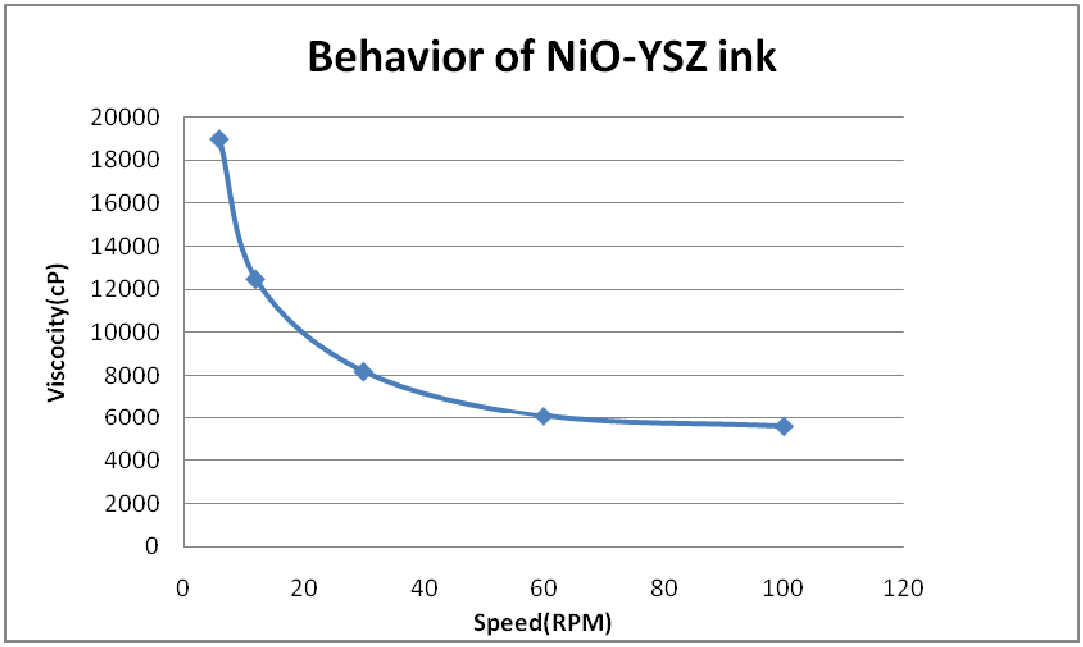

Figure 25 Thixotropic behavior of NiO-YSZ ink

To create porous structures, a fugitive pore former (%wt, %vol, etc.) is typically added to the ink. Pore former materials burn off at sufficiently high temperature, thus leaving voids in the previously occupied volume. Porosity can be controlled by varying the ink composition in three different ways. The first method is to vary the volume fraction of pore former (%wt, %vol, etc.). The second method is to vary the pore former size (e.g. 2 µm – 50 µm). The third method is to vary the pore former shape (spherical, irregular, fibrous, etc.) as shown in Figure 26. These three methods can be combined as needed to create a porous structure of desired pore morphology.

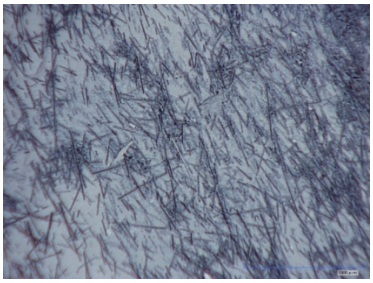

a) Carbon Fibers [r=3µm, l=(50~250 µm)]

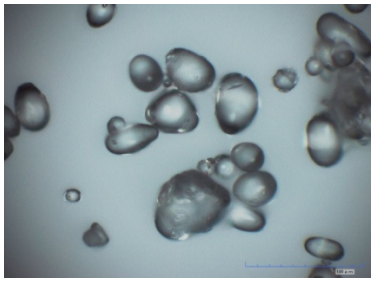

b) Starch Powder (~50µm)

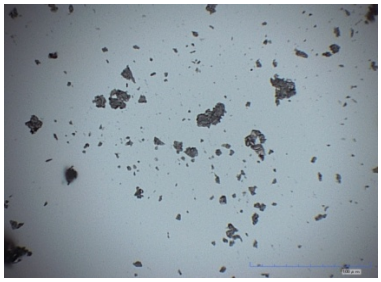

c) Graphite powder (2-15µm)

Figure 26 Various pore forming agents

A list of the materials and their respective suppliers used in this research are provided in Table 16.

Table 16 List of Material and their respective suppliers

Material	Supplier	Powder Sizes (PSD d50)	Comments
Nickel Oxide-YSZ Anode Powder for Coating Applications (NiYSZ-P)	fuelcellmaterials.com	0.5 - 1.2 µm	Anode material
Ink Vehicle (VEH)	fuelcellmaterials.com	Not Applicable	Terpineol
Lanthanum Strontium Manganite (20%) Cathode Powder (LSM20-P)	fuelcellmaterials.com	0.3-0.6 µm	Cathode Material
LSM-YSZ Composite Cathode Powder (LSMYSZ-P) - 50% YSZ by weight	fuelcellmaterials.com	-	Cathode Material
Yttria-Stabilized Zirconia 8 mole% TC Grade (YSZ8-TC)	fuelcellmaterials.com	0.5-0.7 µm	Electrolyte Material
YSZ-8 Substrate Buttons (YSZ-Sub)	fuelcellmaterials.com	NA	Fully sintered 20mm YSZ disk
Graphite powder, natural, microcrystal grade, APS 2-15 micron	Alfa Aesar	2 - 15 µm	Pore former
Graphite Powder (TC307)	Asbury Carbon	2.6 µm	Pore former
Poly Viny Alcohol (PVA)	Alfa Aesar	NA	Binder

3.3 GRADED STRUCTURES

Structures of varying porosity were fabricated using nScrypt's direct write printing technique. Specifically, porosity of a NiO-YSZ anode structure was graded. The anode structure was made porous by adding pore former (%wt. or %vol) to the NiO-YSZ ink. Asbury Carbon graphite powder (TC307) was used as a pore former. The TC307 grade graphite powder has an average particle size of 2.6 µm (PSD d50). The ink compositions used with varying pore former concentrations are listed in Table 17. Figure 27 shows the relationship between pore former weight and volume concentrations in the anode ink composition.

Table 17 Summary of various anode compositions to create structures of different porosity

Sample				NiO-YSZ			GRAPHITE			%Pore former (vol.)
	Total powder weight(g)	%pore former (wt.)	Terpineol (ml)	NiO-YSZ (g)	Density (g/cc)	NiO-YSZ (cc)	Graphite (g)	Density (g/cc)	Graphite (cc)	
1	5.00	0	5.00	5.00	1.55	3.22	0.00	0.13	0.00	0.000
2	5.00	1	5.00	4.95	1.55	3.19	0.05	0.13	0.37	10.50
3	5.00	2	5.00	4.90	1.55	3.15	0.10	0.13	0.75	19.16
4	5.00	3	5.00	4.85	1.55	3.12	0.15	0.13	1.12	26.43
5	5.00	4	5.00	4.80	1.55	3.09	0.20	0.13	1.50	32.61
6	5.00	5	5.00	4.75	1.55	3.06	0.25	0.13	1.87	37.94
7	5.00	10	5.00	4.50	1.55	2.90	0.50	0.13	3.74	56.34
8	5.00	15	5.00	4.25	1.55	2.74	0.75	0.13	5.61	67.21
9	5.00	20	6.00	4.00	1.55	2.57	1.00	0.13	7.48	74.38

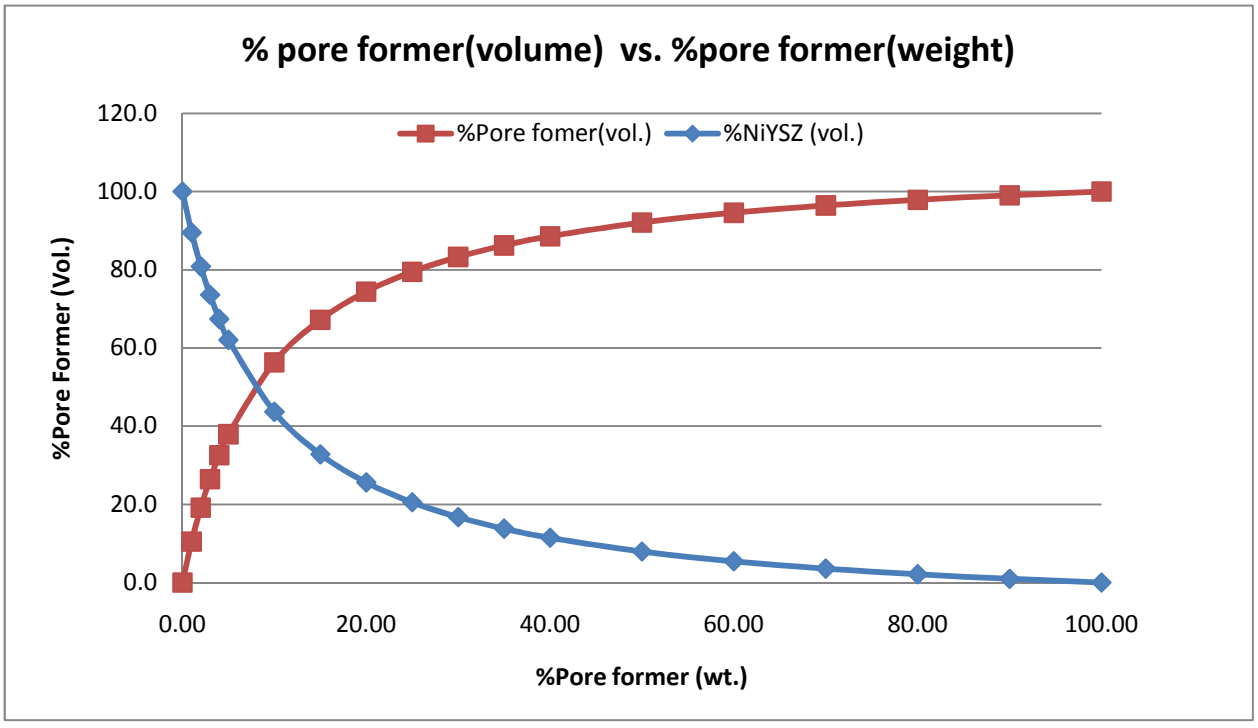

Figure 27 Relation between pore former (%wt) vs. pore former (%volume)

In order to evaluate porosity levels, each ink formulation shown in Table 17 was printed on sintered YSZ substrate to an approximate film thickness of 40 µm using the nScrypt SmartPump micro-dispensing tool. Samples were sintered at 1400°C for 2 hours using a ramp rate of 5°C/minute. The samples were then examined under a Hirox optical microscope in order to qualitatively assess porosity. Micrographs for each experimental condition are shown in Figure 28. There is an increase in porosity from 0%wt. to 5%wt. (0% vol. to 33% vol.) graphite, but the 5%, 10%, 15% and 20% labeled samples appear to be very similar. As is to be expected, there is an upper limit on the amount of pore former that can be added to increase porosity. Beyond this level, additional pore former amounts have no apparent effect.

During the firing process, the solid oxide particles begin to sinter together while the graphite particles are burned off. The SOFC particles can only fuse together if there is contact between adjacent particles. The addition of too much graphite pore former creates space between SOFC particles such that they cannot fuse with each other. As graphite burns off during sintering, SOFC particles collapse on to each other before fusing can begin. Based on experimental results shown in Figure 28, the upper limit on pore former concentration is approximately 5% wt. (~ 38%vol.). Any increase in graphite concentration beyond 5%wt. does not cause a noticeable increase in porosity. It is worth noting that collapsing particles can actually arrange into a denser structure than is achieved with lower volume fractions of pore former. Thus, care must be taken in selecting the amount of pore former to achieve the desired porosity. The size and shape of the pore former also play a vital role.

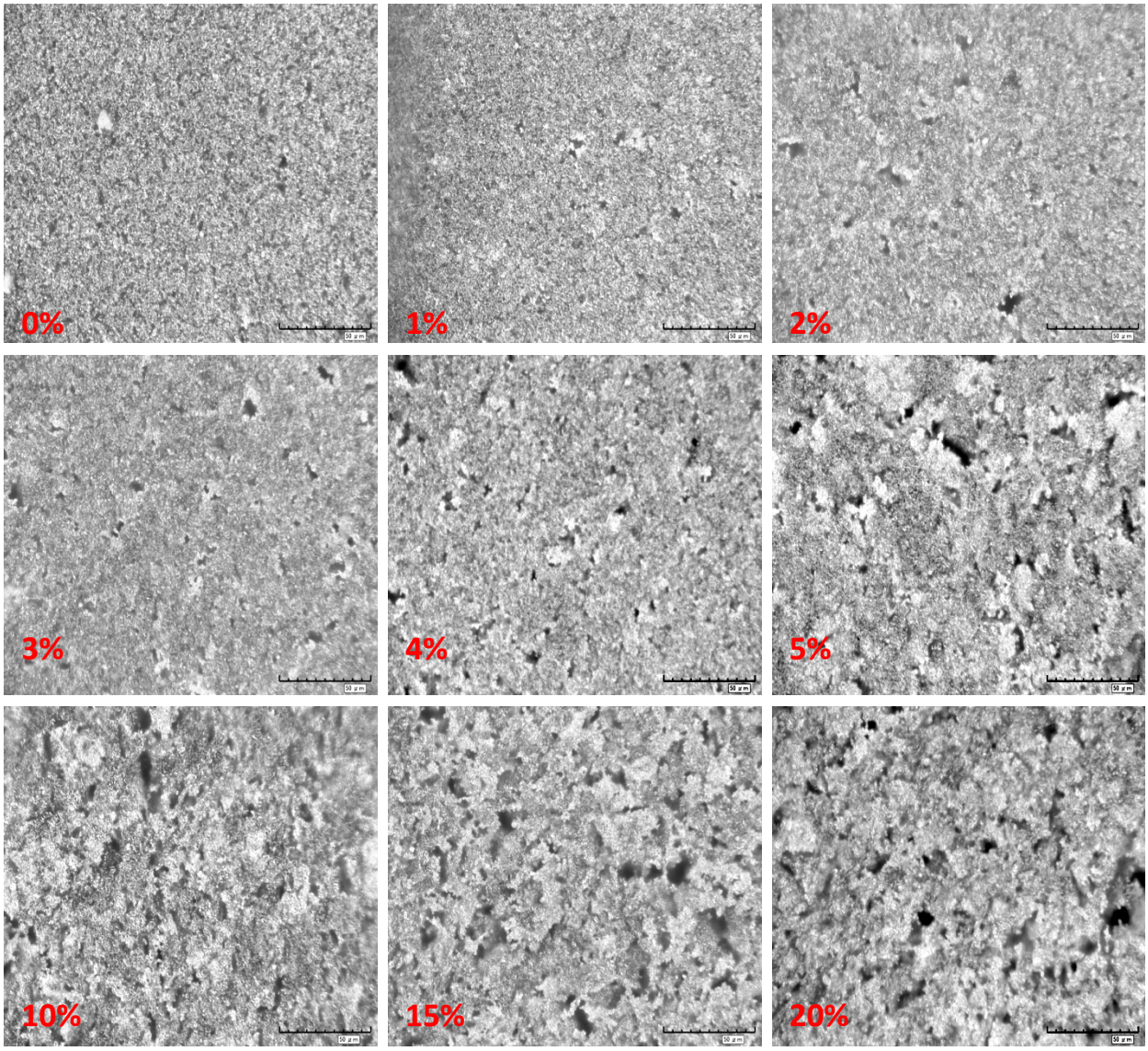

Figure 28 Images of various anodes with different fraction of pore former
(The number labeled is the %weight of pore-former)

Hierarchically graded porous structures can be created using direct-write techniques by printing layer(s) on top of each other in which the amount of pore former is varied from layer to layer. Figure 29 shows 4 layers printed onto a fully sintered YSZ substrate. Two layers at each composition (0% wt. and 15%wt. Alfa Aesar graphite as pore former) were printed via the nScrypt direct write method. The total layer thickness was 60 µm with average thickness of ~15 µm per layer.

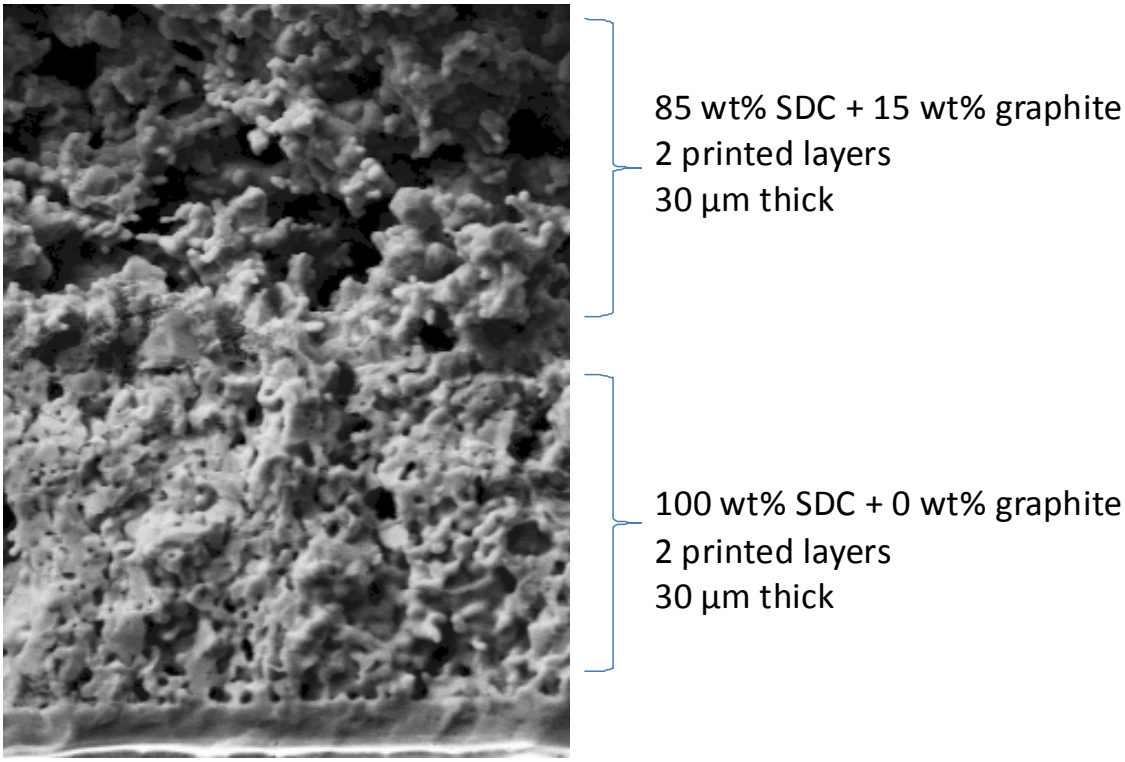

Figure 29 Graded porous Semarium Doped Ceria (SDC) structure (4 layers printed at 2 different compositions)

3.4 GRADED STRUCTURE WITHIN A LAYER

While the preceding section addressed the topic of grading pore structure between layers, the direct write method is also suitable for grading the composition or porosity within a plane/layer. This approach can be used to create gas flow channel in a SOFC electrodes.

The tool set-up for grading structure within a layer is shown in Figure 30. A 3 way-luer connector was used; two ports are used as inputs from the syringes and the third one used as an output where the ink extruded through a nozzle. By controlling the pressure on the syringes, different proportions of the two inks can be extruded side-by-side. For instance, if one of the inks is a fuel cell material and the other a fugitive material, the fugitive material will burn off during sintering leaving long channels behind. This methodology worked fairly well for inks with lower viscosities, but high viscosity experiments performed here were unsuccessful due to the large

amount of backpressure. When pressure on one reservoir is significantly higher than the others, then ink backflows from one syringe barrel to the other rather than coming out of the nozzle. A positive displacement dispensing technique is therefore suggested to improve the process

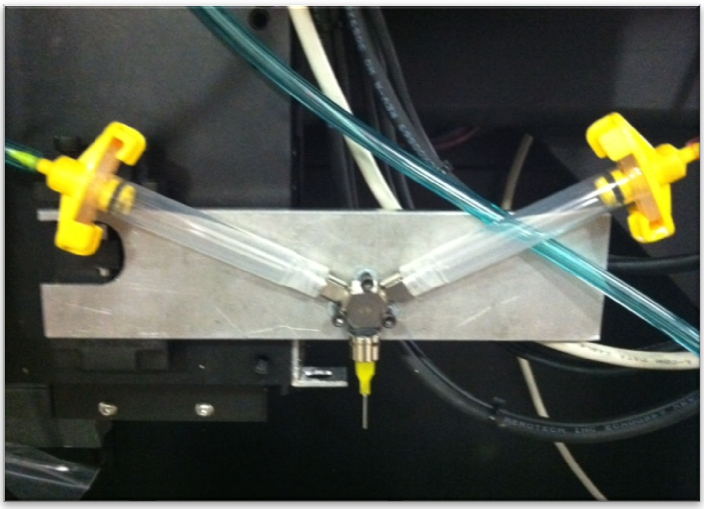

Figure 30 Tool setup to vary composition within a layer/plane

Although attempts to grade composition within a plane using pneumatic micro-dispensing were not successful, Figure 31 conceptually demonstrates the principle. This was done via a two step process using nScrypt single material Smartpump. First, lines consisting of ink with 2% pore former concentration were printed with some spacing in between the lines on a die-pressed NiO-YSZ unsintered disk. Then, the ink with 5% pore former concentration was printed in the space between the already printed lines. The structure was then sintered at 1400°C for 2 hours and inspected under a Hirox optical microscope. The image below shows a post sintered top-down optical micrograph with graded porosity/composition within a layer. The less porous region to the left consists of NiO-YSZ with 2% pore former, and the more porous region to the right consists of NiO-YSZ with 5% pore former.

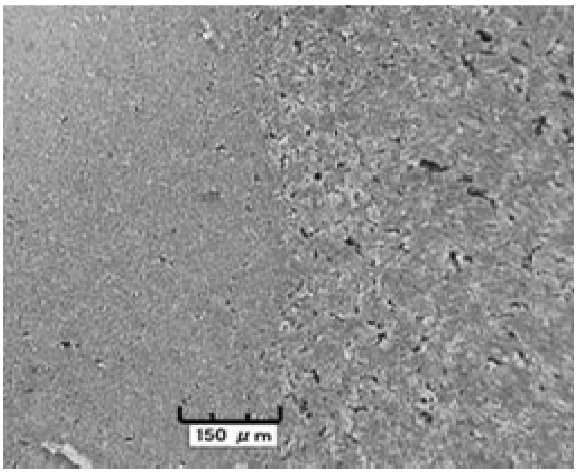

Figure 31 Graded Porosity/Composition – within a layer

3.5 SOFC FABRIACTION USING DIRECT WRITE METHODS

An electrolyte-supported button cell based on YSZ electrolyte were fabricated using nScrypt's direct write micro-dispensing method. The electrolyte-supported cell based on YSZ consists of an anode layer, and two cathode (LSM/YSZ and LSM) layers.

Fully sintered 20mm YSZ-8 disks (Fuel Cell Materials) were used as the electrolyte support layer. One anode layer and two cathode layers were printed in the configuration shown in Figure 32. The cathode consisted of two distinct printed layers containing LSM/YSZ and LSM with pore former respectively. The pore former was added to make the structures more porous.

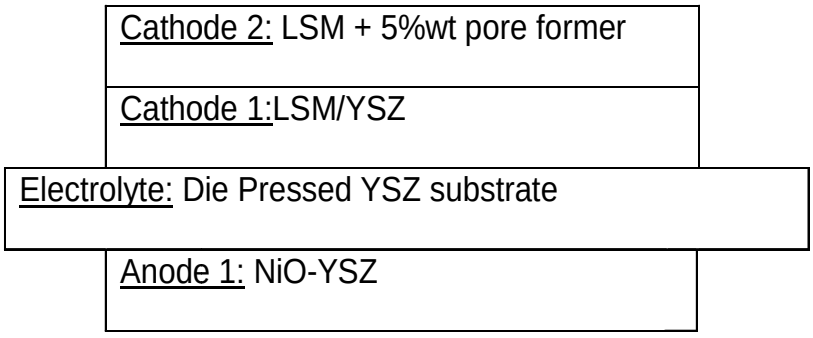

Figure 32 Schematics of a electrolyte-supported cell

First, the LSM/YSZ ink was printed onto the disk and dried under a heat lamp for one hour. A second layer of LSM with 5% Alfa Aesar graphite ink was then printed and dried under a heat lamp for one hour. The cell was then fired at 1000°C for 2 hours with a ramp speed of 5 °C per minute. On the back side of the disk, a layer of NiO-YSZ ink was printed and dried under a heat lamp for one hour. The button cell was then co-sintered in an MTI furnace (KSL-1500X) at 1400°C for 5 hours with ramp rate of 5°C per minute. The diameter of cathodes and anode printed were 15mm each.

A 125 µm inner diameter ceramic nozzle was used to print all layers of this button cell using the nScrypt machine. The dispensing height was kept at ~50 µm for all layers. Table 18 summarizes the ink composition and the printing process parameters for the electrolyte supported cell.

Table 18 Electrodes ink composition and process printing parameters for Electrolyte-supported cell

Structure	Composition		3D Direct Write Tool Parameters			
			Speed (mm/s)	Pressure (PSI)	Valve Opening (mm)	Stepover (µm)
Cathode 2	4.5 grams LSM + 0.5 grams Alfa Aesar Graphite+ 4mL Ink Vehicle (VEH)		16	5	2.3	200
Cathode 1	8.2 grams LSM/YSZ + 4mL VEH		10	5	2.3	200
Anode 1	10 grams NiO-YSZ + 4ml VEH		10	6	2.3	150

Figure 33 shows the resulting electrolyte-supported cells that include an 80 µm thick cathode, a 40 µm anode and a 250 µm electrolyte.

a) Electrolyte supported button Cell (20mm electrolyte, 15mm electrodes)

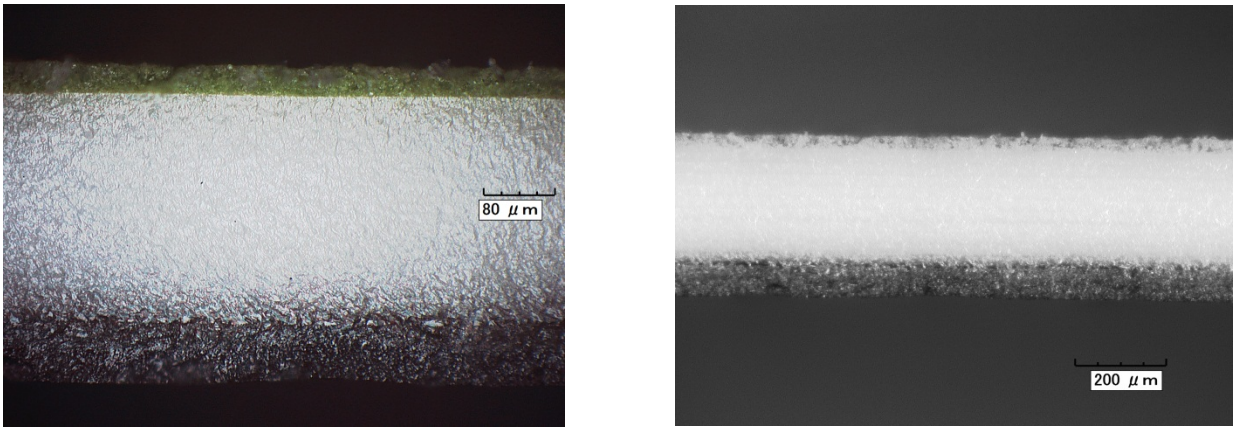

b) X-section of electrolyte-supported cell

Figure 33 Electrolyte-supported cell

The testing of the button cells were done at the SOFC Center of Economic Excellence located in the Horizon Research building at University of South Carolina (USC), South Carolina, U.S.A. For testing the button cells, the samples were prepared by brushing the anode and cathode sides with platinum slurry (Haraeus Cl11-5349) which serves as the current collector. The button cell was co-fired at 950°C for 0.5 hours at a ramp up rate of 2°C per minute. Platinum wire was preferred due to the high testing temperature and to endure longer test cycles. Finally, ceramic sealing paste was brushed around the perimeter of the cell to seal it to the ceramic tube prior to testing.

The cell was heated to 600°C in hydrogen to reduce NiO to Ni in-situ. The cell was stabilized at 600°C for 2 hours before the electrochemical test was performed. Electrochemical characterizations were performed at a temperature of 800°C under ambient pressure. Fuel cell performance was measured with a Versa STAT 3-400 test system (Princeton Applied Research). Hydrogen (3%H_2O) was used as fuel (40 ml per minute), and stationary air was used as the oxidant. AC impedance was measured at open cell circuit in the frequency range from 0.05 Hz to 100 kHz on a potentiostat/galvanostat with built-in impedance analyzer.

An open circuit voltage (OCV) of around 1 Volt at 800°C was achieved which is comparable to other SOFC fabrication methods. However, the polarization resistance was excessively large as shown in Figure 34. This may be due to the fact that the cathode was sintered at 1400°C. It is likely that a chemical reaction between LSM and YSZ formed a less conductive La-Zr-O phase at that temperature. Calcinating the cathode at no more than 1200°C along with electrode thickness <100 µm should improve the performance of this cell.

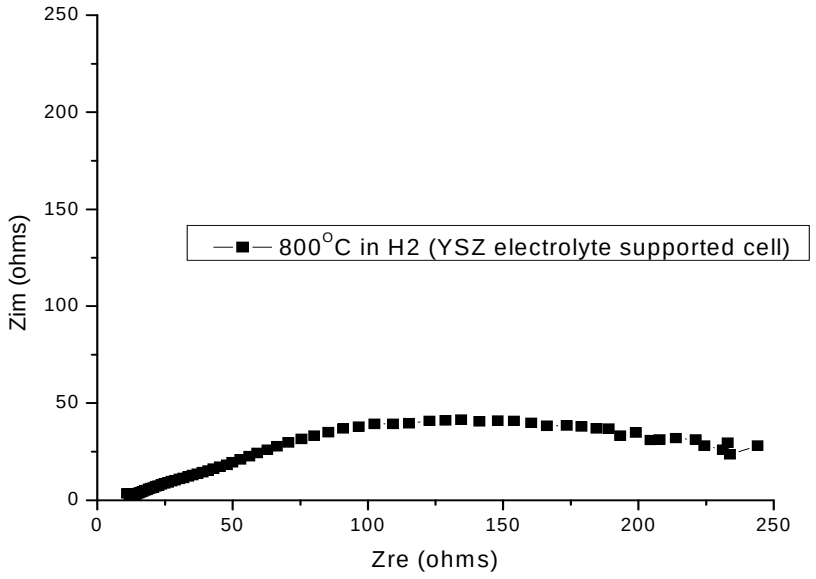

Figure 34 Impedance spectra of YSZ-electrolyte supported cell at 800°C in wet H2.

3.6 ENGINEERED STRUCTURES

The bi-electrode supported cell (BSC) structure produced via freeze tape casting has very unique properties that potentially offer high power density and efficiency. A single cell BSC has already been demonstrated; however, the fabrication and performance of a multi-cell stack still remains a challenge [60].

Despite the many intriguing aspects of the freeze tape cast structure, one of the challenges with the process is the fact that the pore macrostructure is linearly aligned with the direction of freeze tape casting. During sintering, the shrinkage is therefore much greater in the direction of the channels than it is in the direction perpendicular to the channels. Likewise, the structure is much weaker in the direction orthogonal to the channel orientation. One of the principle aims of this research is therefore to develop a process capable of replicating the unique freeze tape cast structure while also providing the flexibility to produce ribs and channels in any desired geometric pattern.

For this research, direct write techniques have been used to create a BSC like structure with arbitrarily complex geometry. By laying down lines on top of each another, a significant height can be built up by this process. If these lines are printed at some step-over distance, then a structure loosely comparable to that of the freeze tape cast BSC structure can be fabricated.

3.6.1 Initial Trials for Micro-Extrusion of Vertical Ribs

Up to this point in the thesis, the direct-write technique has been used to print and fill circular anode or cathode layers. In order to demonstrate feasibility of direct-write methods for production of BSC-like structures, it is necessary to stack single-wide lines of ink on top of one another while avoiding slump or collapse of the printed stack while the ink dries.

To do this, the anode material (NiO-YSZ) has been used. The ink was made in the ratio of 12 grams NiO-YSZ per every 3ml VEH (Terpineol). The ink was thoroughly mixed in a THINKY mixer for 20 minutes @ 2000 RPM. The ink was then transferred to a 3cc syringe and placed in the nScrypt tool.

A toolpath was written to print lines with various step-over distances. The step-over settings were 400, 300, 280, 250, 230 and 200 µm (see Appendix A for an example of a machine code). A fully sintered YSZ disk was used as a substrate. A first layer was printed on the YSZ disk, and the dispensing height was increased by 70µm. A second layer was then printed. The dispensing height was increased by another 70µm and a third layer printed. A total of 11 layers were printed with +70 µm dispensing height adjustments per layer. The process parameters used are summarized in Table 19. A 125 µm ID ceramic nozzle was used for extrusion.

Table 19 Process parameter for a BSC like structure

Number of layers	Dispensing Height (mm)	Speed (mm/s)	Pressure (PSI)	Stepover (µm)	Valve Opening (mm)
1	-59.47	1.5	40	400, 300, 280, 250, 230, 200	2.4
2	-59.40	2.0	40		2.4
3	-59.33	2.0	40		2.4
4	-59.26	2.0	40		2.4
5	-59.19	2.0	40		2.4
6	-59.12	2.0	40		2.4
7	-59.05	2.0	40		2.4
8	-58.98	2.0	40		2.4
9	-58.91	2.0	40		2.4
10	-58.84	2.0	40		2.4
11	-58.77	2.0	40		2.4

The sample was then dried under a 250W heat lamp at a distance of 2 feet for one hour. The height of the green unsintered structure was ~810µm when measured with the Hirox Microscope (KH-7700). The sample was then sintered at 1400°C for 2 hours at a ramp up rate of 5°C per minute. The height of the sintered sample was ~650 µm (Figure 35). The walls of the

resulting ribs are smooth and vertical and show no obvious signs of slumping. The rib width for the processing conditions was roughly 100µm.

Figure 36 shows results from the rib and channel trials in which the step-over distance was varied. The rib width was about 100 µm. The smallest spacing of about 130µm was observed for a step-over distance of 230µm and the largest channel width of approximately 300µm was observed for 400µm step-over setting. The average thickness of each individual layer post sintering was approximately 60µm. The height shrinkage rate was (810-650)/810 ~ 20%.

One problem encountered was that the printed ribs severely warped along their length during the sintering process and delaminated from the substrate. This is likely caused by two issues. The first is that the substrate was fully sintered prior to the sintering process. When the printed ribs shrink on a "pre-shrunken" substrate, it is likely that there will be significant stress between the ribs and the substrate. These stresses can be minimized by printing on an un-sintered die-pressed disk as demonstrated in the next experiment. The second issue is that the shrinkage takes place primarily along one axis parallel to the direction of the ribs. This leads to warping along the lengthwise direction of the ribs as is commonly seen with the freeze tape casting structure. This issue can be addressed through printing of non-linear rib geometries.

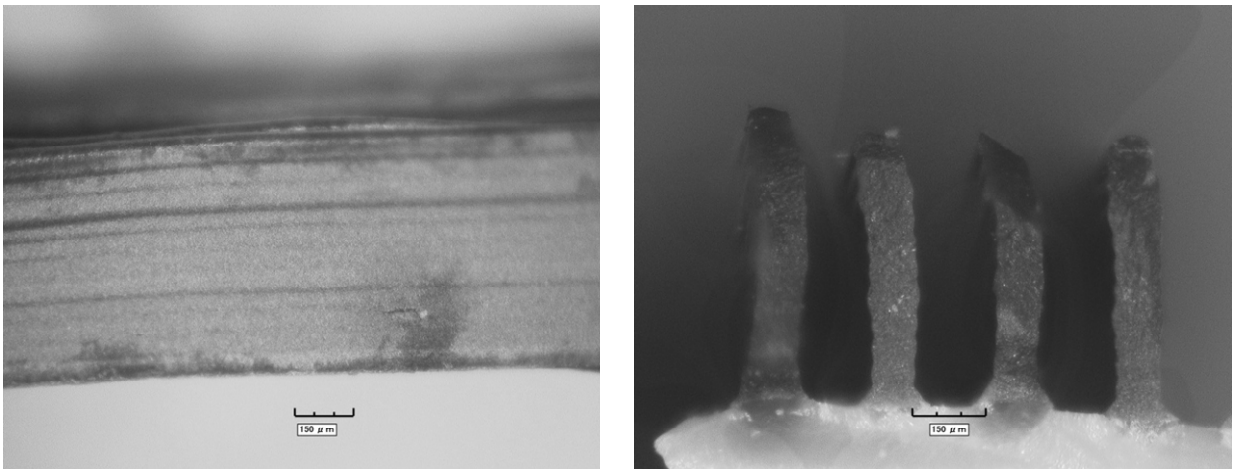

Figure 35 3D printed BSC like structure: side-view of the line (left) and X-section (right)

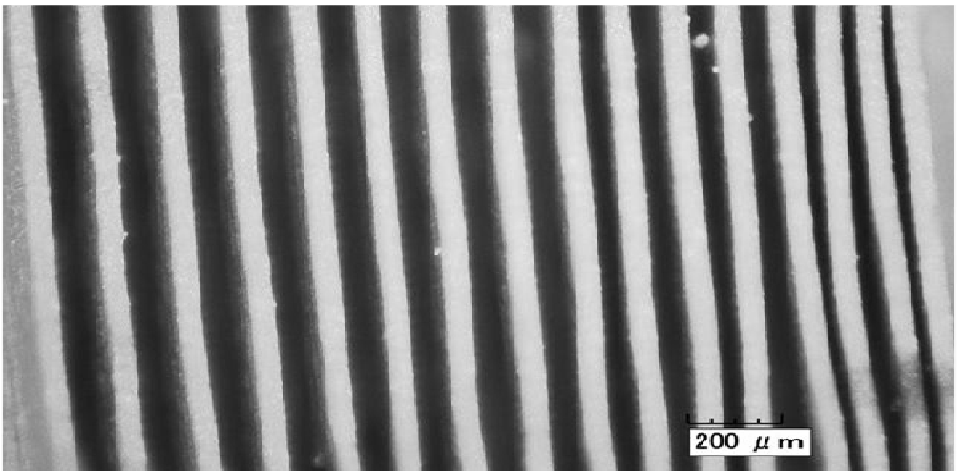

Figure 36 Lines at different step-over distances

Figure 36 show the variation in the channel width as step-over is varied. Issues arise when the step-over is decreased, as seen towards the right side of the image where lines are getting closer and closer. There is a limit on how close the lines can be printed before they touch one another. As mentioned previously, the dispensing height is a critical parameter. As the ink used is highly viscous, the dispensing height becomes ever more important. The dispensing height of +70µm per layer was used in this experiment. In trials where the height was less than 70µm, the nozzle tended to clog up and produced inconsistent extrusion with blobs of ink dispensing randomly during the printing process. With a 125 µm nozzle, the diameter of the extrudate is

also 125 µm. For gap distances less than 125 µm, the extrudate is necessarily being compressed to a certain extent as it exits the nozzle. Below 70 µm layer increments, the ink faces excessive backpressure resistance during the extrusion that leads to inconsistent print results. For layer heights greater than 70µm, the extruded ink tended not to adhere very well to the previous layer, and misalignment of subsequent print layers was common. This was likely due to the poorly attached extrudate getting pulled towards one side of the already printed line. In some cases, the extrudate was not continuous. In summary, initial trials indicated that successful printing of smooth vertical built-up ribs is heavily dependent upon layer thickness which controls both adhesions to previous layers as well as the shape of the compressed extruded bead.

3.6.2 Micro-Extrusion of Vertical Ribs On Unsintered Substrates

The next step was to address the problem of warping in the printed ribs. For this purpose, a 15mm anode disk was die-pressed. The BSC like lines were printed on the die pressed disk and then co-sintered.

The powder constituents for the anode disk (substrate) were 8 grams NiO-YSZ powder and 2 grams graphite (TC307). The powder was mixed in a VQN high speed ball mill for 20 minutes. Several drops of PVA solution, created by mixing 5 grams with PVA with 100 ml distilled water, were added to the mixed powder. The powder was allowed to dry and was then die pressed at 3 metric tons for 25 seconds.

The ink composition for this experiment was slightly changed by adding graphite powder (Asbury TC307). The new ink composition consisted of 12 grams NiO-YSZ, 0.5 grams graphite (4% wt.) and 3ml VEH (Terpineol). The reason for adding the graphite was to make the ink more viscous and the printed lines more porous (as graphite burns off during the sintering process). Instead of printing long straight lines as in the previous experiment, a series of nested concentric

circles having a step-over of 250 µm were printed. This was done to ensure symmetric shrinkage stresses and to produce a patterned structure with greater mechanical strength in all directions.

A tool path was written for the nScrypt machine to print concentric circles. The initial outer diameter was 6mm (6000 µm) and each successive circle was offset inward by 250 microns (i.e. step-over of 250µm). Lines were printed on the un-sintered die pressed NiO-YSZ anode disk. Concentric rings for the first layer were printed, and the dispensing height was then increased by 50µm. A second layer of concentric rings were then printed on top of the first layer of rings. The dispensing height was then increased by another 50µm and a third layer printed. A total of 6 layers were printed with +50 µm dispensing height adjustments. The process parameters for the above experiment are tabulated in Table 20. The 75 µm ceramic nozzle was used for extrusion.

Table 20 Process parameter for a BSC like structure with step-over of 250µm

Number of layers	Dispensing Height (mm)	Speed (mm/s)	Pressure (PSI)	Step-over (µm)	Valve Opening (mm)
1	-58.90	0.75	46	250	2.4
2	-58.85	0.75	46		2.4
3	-58.80	0.75	46		2.4
4	-58.75	0.75	46		2.4
5	-58.70	0.75	46		2.4
6	-58.65	0.75	46		2.4

The sample was then dried under the 250W heat bulb at a distance of 2 feet for one hour. The height of the green (unsintered) structure was ~378µm when measured with the Hirox Microscope (KH-7700). The sample was then sintered at 1400°C for 2 hours at a ramp up rate of 5°C per minute. The height of the sintered sample was ~270 µm (Figure 37). The sample along with the die-pressed disk showed no warping and no delamination. Table 21 below provides a summary of the results.

Table 21 Summary of results of BSC like concentric circles

	Pre-Sintered	Post-Sintered	Shrinkage (%)
Die pressed disk	15 mm	12mm	20
6mm circle diameter	6000 µm	4770 µm	21
Height	378 µm	290 µm	23
Individual rib width	98 µm	75 µm	23
Individual channel width	134 µm	130 µm	3
Stepover (line+channel)	250 µm	206 µm	18

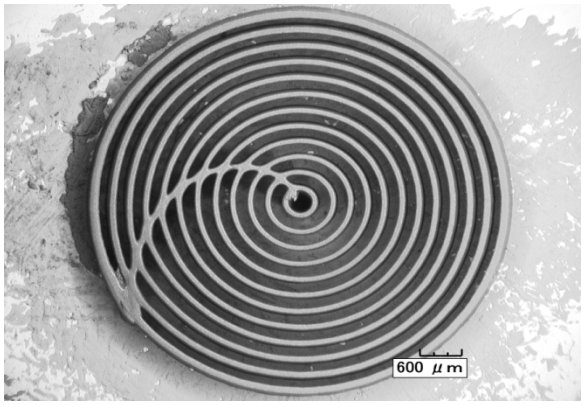

a) Pre sintered (Magnification 35X)

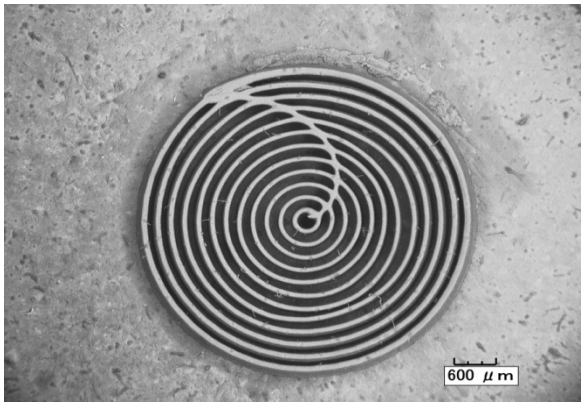

b) Post-Sintered (Magnification 35X)

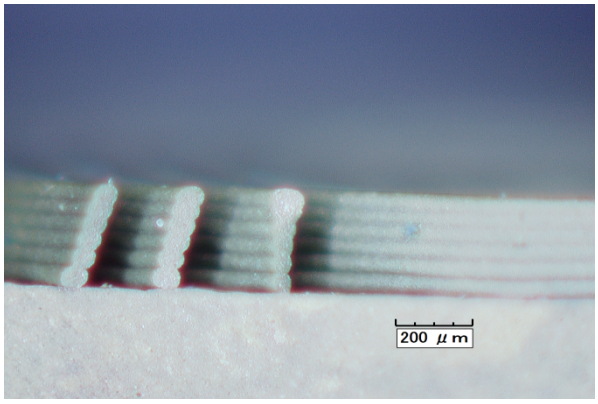

c) X-section (Post Sintered)

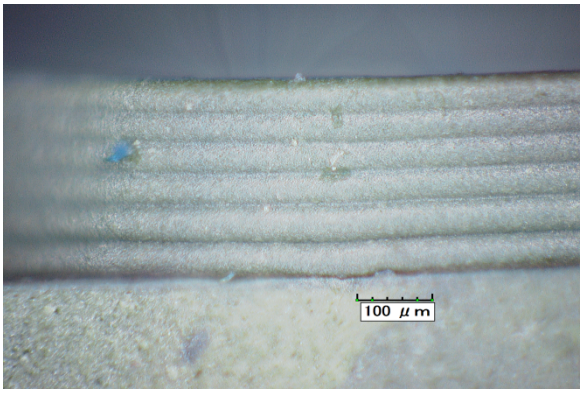

d) Side-view of the line (each layer is visible)

Figure 37 BSC like concentric circle structures

This demonstrates the potential of direct-write printing to produce engineered electrode structures with low tortuosity and balanced shrinkage stresses. Future efforts should focus on minimizing rib and channel widths in order to increase the total available surface area. In the

next experiment, another concentric ring structure is fabricated with reduced step-over distance in an attempt to determine the minimum channel width between ribs and to illustrate the repeatability of the process.

3.6.3 Increasing the Area Density of Microextruded Ribs

The steps for this trial were identical to the settings used to print the concentric ring structure. The only change was that the step-over distance for the concentric circles was varied in an attempt to determine the minimum channel width between ribs. Step-over distances used were 180, 150, 120 and 100µm. An 8 layer structure and a 16 layer structure were fabricated. The 75 µm ceramic nozzle was used for extrusion. Table 22 summarizes the process parameters used for each experiment.

Table 22 Summary of process parameters for 100,120,150 and 180 µm step-over concentric circle

Layer Number	Dispensing Height (mm)	Speed (mm/s)	Pressure (PSI)	Step-over (µm)	Valve Opening (mm)
1	-58.90	0.75	46	180, 150, 120, 100	2.4
2	-58.85	0.75	46		2.4
3	-58.80	0.75	46		2.4
4	-58.75	0.75	46		2.4
5	-58.70	0.75	46		2.4
6	-58.65	0.75	46		2.4
7	-58.60	0.75	46		2.4
8	-58.55	0.75	46		2.4
9	-58.50	0.75	46		2.4
10	-58.45	0.75	46		2.4
11	-58.40	0.75	46		2.4
12	-58.35	0.75	46		2.4
13	-58.30	0.75	46		2.4
14	-58.25	0.75	46		2.4
15	-58.20	0.75	46		2.4
16	-58.15	0.75	46		2.4

During the printing process, the ribs printed with just a 100 µm step-over distance actually touched each other; hence no channels were created with a 100 µm step-over. The smallest channel was observed during printing with a 120 µm step-over distance. At this setting, rib

widths for 8 layers and 16 layers were 335 and 600 µm respectively (Figure 38). The average thickness per layer was approximately 40 µm. The smallest channel width observed was 20 µm. The predicted rib and channel dimensions based on shrinkages (see section 3.6.2) from earlier trials agree very well with the actual rib and channel dimensions as shown in Table 23. While the rib width was unchanged from the previous experiment (~75 µm), the channel width was successfully decreased from 130 µm down to 20 µm. The impact of this change on active surface area in the electrolyte layer is substantial and is discussed in the next section.

Table 23 Predicted profile of the BSC like structure with step-over of 120 µm

	Pre-Sintered	% shrinkage	Predicted post-sintered		Actual post-sintered	Variability (%)
Die pressed disk diameter	15 mm	20%	12 mm		12 mm	~ 0
Height (8 layers)	426 µm	23%	328 µm		335 µm	~2
Height (16 layers)	750 µm	23%	578 µm		600 µm	~ 4
Individual rib width	98 µm	23%	75 µm		78 µm	~ 4
Individual channel width	22 µm	3%	21 µm		20 µm	~ 5
Step-over (line + channel)	120 µm	18%	98 µm		98 µm	~ 0

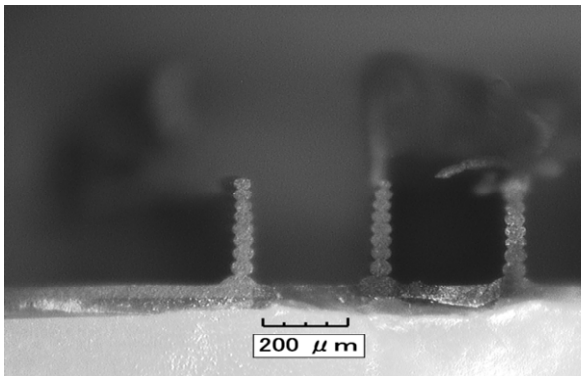

a) 8 layers

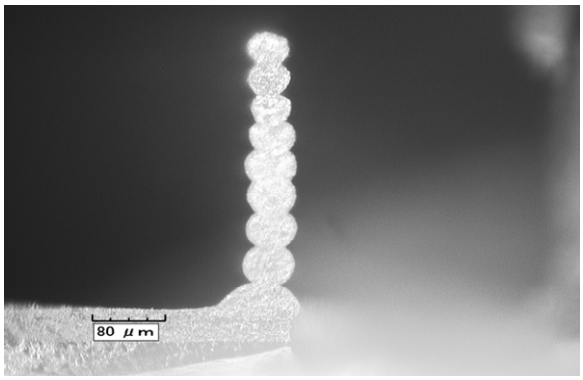

b) 8 layers

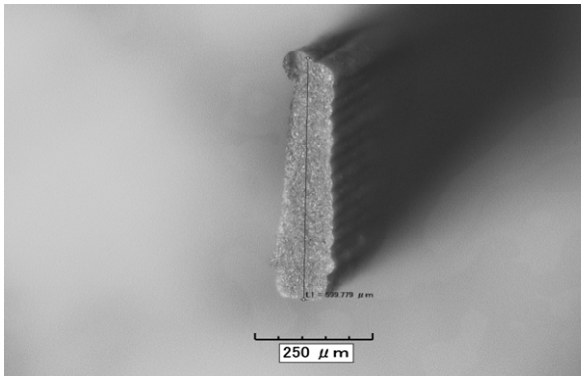

c) 16 layers

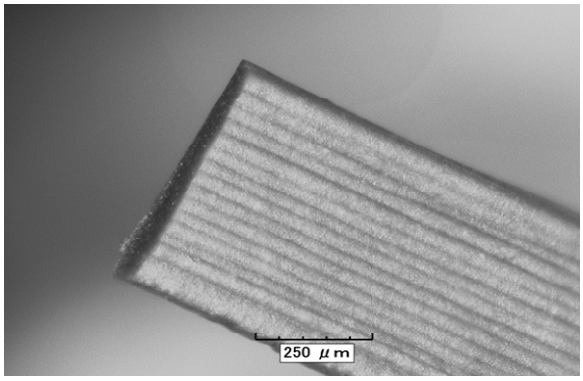

d) 16 layers (side-view)

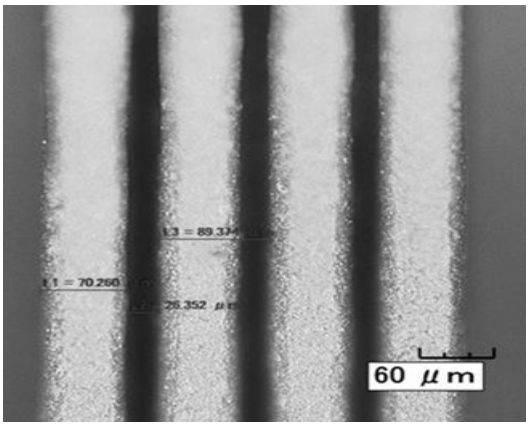

e) **Top-down view of lines printed (Post sintered) at a step-over distance of 120µm**

Figure 38 Structured Electrodes: 8 layers and 16 layers

3.6.4 Analysis

Efficiency in a SOFC is a function of a very large number of factors. As previously discussed, the nature of porosity in the anode and cathode layers greatly influences things such as

active surface area, gas permeability, and conductive path length which affect ohmic losses. Sections 3.5.1 through 3.5.3 have given details on how the architecture of an electrode can be manipulated via the microextrusion based direct-write process. In this section, the effect of those changes on area density of the electrode is analyzed.

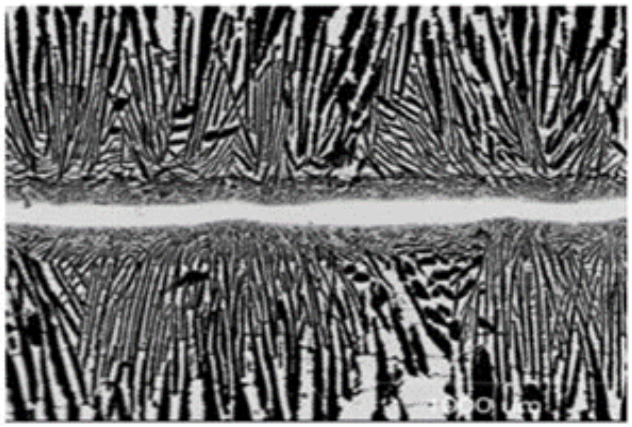

Figure 39 BSC structure [27]

Using direct-write printing, it has been demonstrated that a reasonable approximation to the freeze tape cast BSC structure shown in Figure 39 can be produced. Two important observations can be made. The first is that the rib and channel widths can be varied within a certain range through proper selection of process parameters. The second is that the ribs themselves can be modified to produce ribs with either smooth vertical walls or scalloped vertical walls as shown in Figure 40. All of these structures provide high surface area with low tortuosity, which is highly desirable for a variety of reasons.

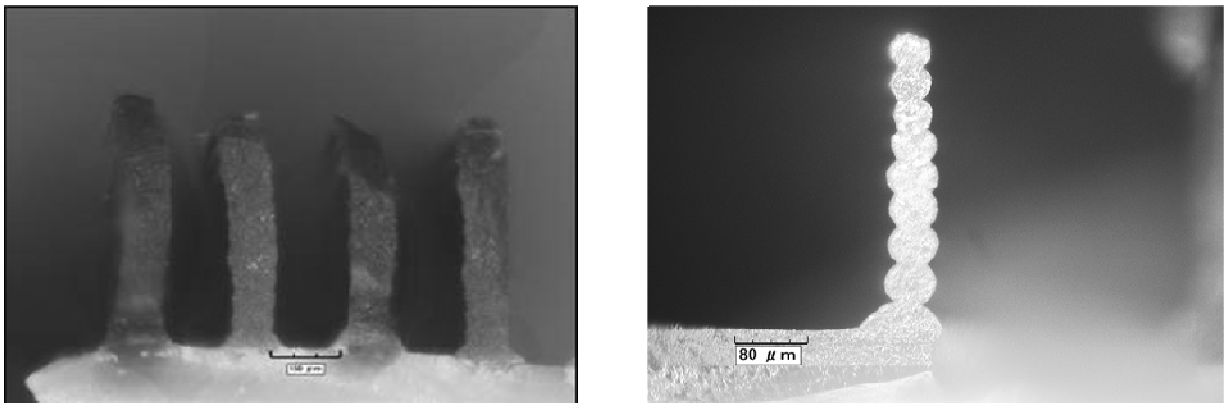

a) Vertical walled lines **b) Scalloped walled lines**

Figure 40 Side-by-side comparison of engineered BSC like structure

In the case where a rib has smooth vertical walls, the surface area and porosity can be analyzed as a function of rib and channel geometry as follows (Figure 41). Assuming that the ribs are approximated by rectangles with height (*h*), line width (*l*), channel width (*w*), length of line (*len*) and number of lines (*n*):

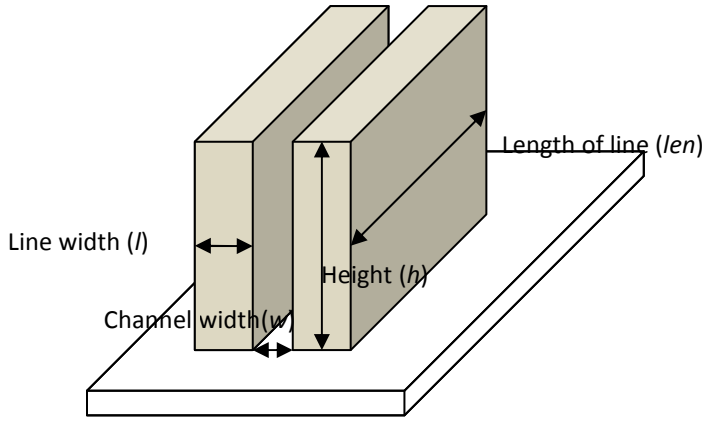

Figure 41 Modeling of smooth vertical walls

The total surface area calculated above includes all six sides of the ribs and assumes that the structure are fully dense, whereas the top/bottom and front/back faces would be covered in a real cell and the structure will be porous. So, the actual total surface area is:

$$Actual\ total\ surface\ area \geq 2 * n * h * len, where\ n = \frac{Area}{(l + w)}$$

Since the structure is actually porous, the actual total surface area will go up depending on the chosen porosity of the ribs. This arrangement provides channels for the gases to easily flow into. It also provides a better means for solution infiltration techniques commonly used for cathodes.

Using typical values for an anode layer (say a 20mm x 20mm square button cell with h =500µm thick), Figure 42 shows the effect of channel width *(w = 20 to 150*µm) on actual total surface area for *l = 50, 75 and 100* µm.

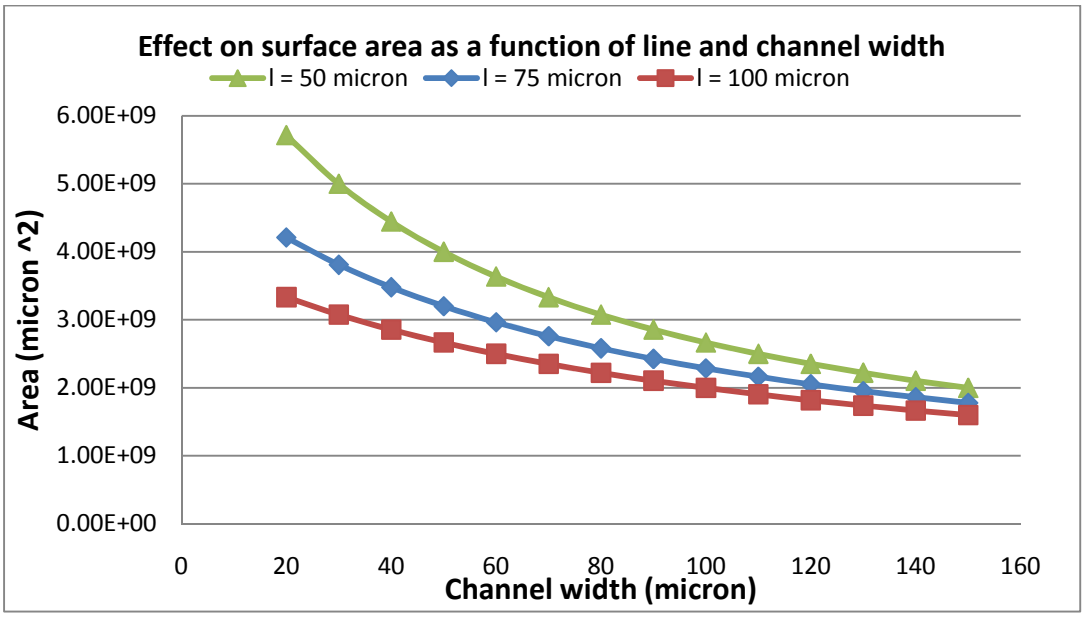

Figure 42 Effect on surface area as a function of channel width

In Figure 35, the ability to produce ribs having smooth vertical sidewalls was demonstrated. Note that the sidewalls shown in Figure 37 (concentric rings) exhibit scalloping due to a slightly smaller layer thickness that compressed the extruded bead. A rib having scalloped side walls has a greater amount of surface area than ribs with smooth walls. The degree to which process parameters influence surface area in the printed ribs is therefore analyzed.

The surface area of the rib is a function of extruded bead diameter and the layer thickness. When a viscous paste is extruded through a round orifice, it will take on a cylindrical shape that may be less than, approximately equal to, or greater than the orifice diameter. If the gap between the orifice and the substrate is less than the bead diameter, then the bead will be "squashed" to a certain extent. By depositing multiple beads on top of each other to create a fin structure, it is possible to create a wall having scallops. The net effect is a wall whose surface area is greater than that of a perfectly vertical wall.

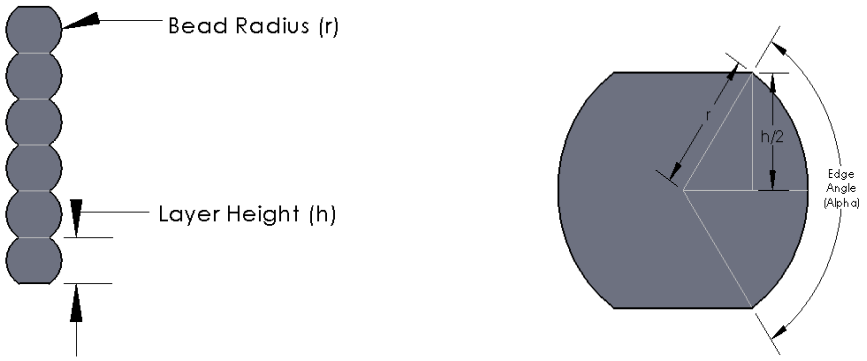

With a perfectly vertical wall, the edge length equals *h*. With a scalloped wall as shown above, the scalloped edge length can be calculated as a function of the bead radius (*r*) and layer height (*h*). The angle that is swept by the scalloped edge (α) is determined as follows:

$$\sin\left(\frac{\alpha}{2}\right) = \frac{h/2}{r}$$

$$\alpha = 2\sin^{-1}\left(\frac{h}{2r}\right)$$

Since the circumference of a circle having radius r is πd, the length of the arc swept through an angle α on that circle is determined as follows:

$$Edge\ Length\ (one\ side) = \frac{\alpha}{360}\pi d = \frac{\sin^{-1}\left(h/_{2r}\right)\pi d}{180}$$

Table 24 computes the scallop edge length as a function of layer height and radius (assuming that a radius = 50 µm). If the scallop edge length is compared with a vertical wall edge length of h, then the percent increase in edge length grows rapidly as the layer height increases relative to a given bead radius. Since surface area is simply edge length multiplied by the length of the rib, the increase in overall electrode surface area scales directly with the increase in edge length. This increase in surface area is also achieved with very little influence on the tortuosity of the electrode, but could have a negative impact on the mechanical properties of the structure.

Table 24 Scalloped Edge length as a function of layer height and radius

Layer Height (h) (µm)	Radius (r) (µm)	Scallop Edge Length (µm)	Percent Increase In Edge Length
50	50	52.4	4.7%
60	50	64.4	7.3%
70	50	77.5	10.8%
80	50	92.7	15.9%
90	50	112.0	24.4%
100	50	157.1	57.1%

By way of example, the 8 layer structure shown in Figure 43 has an average diameter of 46.5 µm ± 5.5 µm and an average layer height of 36.4 µm ± 4.8 µm (Table 25). The ink was extruded though a 75 µm nozzle. The ratio of the bead radius of the extruded layer to the nozzle size is 0.62 (= 46.5/75). Using the formula above for calculating the edge length, an increase of 14.8% surface area was calculated for scalloped line when compared to vertical wall.

$$Vertical\ height = 36.4\ \mu m$$

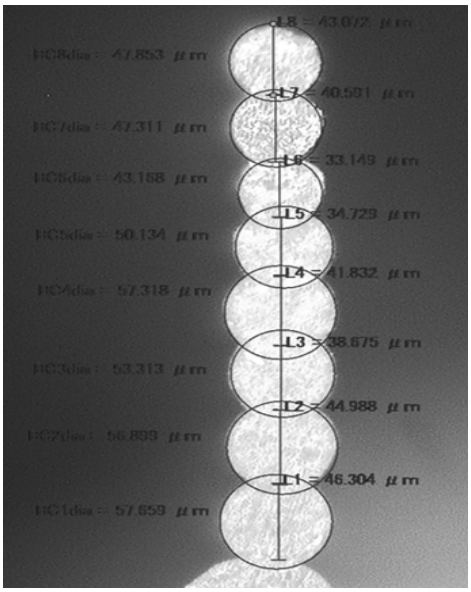

Figure 43 8 layer structure

Table 25 8 layer structure height and diameter summary

Layer	Diameter(µm)	Height(µm)
1	58	46
2	57	45
3	53	39
4	57	42
5	50	34
6	43	33
7	47	41
8	48	43
Average	**46.5**	**36.4**
Std. dev.	**5.5**	**4.8**

In practice, the bead radius is a function of the printing parameters and the ink composition. By adjusting process parameters (speed, pressure and dispensing height), bead radius and the degree of scalloping can be engineered within limits.

Smaller channels and thinner lines can further be achieved by adjusting the following process parameters and using other alternate methods:

1) Process Parameters:
    a. Make the ink thicker (higher ink viscosity) as it will not flow out as much on the substrate.
    b. Print on a cold substrate (below freezing temperature of ink) to minimize the flow out of ink.
    c. Print on a substrate with a higher surface tension so that the ink does not flow out.
    d. Print via a smaller diameter nozzle if possible. The use of smaller sized powders may be needed to prevent clogging.
    e. Apply less pressure to extrude the ink out of the ceramic nozzle as less pressure reduces the volumetric flow rate during printing.
    f. Print with a higher translation speed to "stretch" the bead and get thinner lines.
    g. Adjust the dispensing height where minimum flow rate of ink is achieved.
2) Alternate Methods
    a. Co-extrusion: This process prints 2 different ink pastes through a nozzle at the same time with little or no mixing. If one is a fugitive material and the other the fuel cell material, the stripe of fugitive material will burn off leaving behind a channel. This way finer channels and ribs can be created. By controlling the ratio of the two materials, various ratios of lines to channels can be achieved.
    b. Use alternative direct-write technologies: Optomec's Aerosol Jet (AJ) Technology is capable of producing finer feature sizes (< 15µm). The advantages of the AJ process include: feature sizes to 15 microns, thin layer deposits from 100 nm, material

viscosities from 1- 1,000 cP, nanomaterial deposition capability, ability to print on non-planar substrates, and low temperature processing. A drawback of using a raster-based technology with smaller features sizes is that the deposition time can increase dramatically.

CHAPTER 4: SUMMARY AND CONCLUSIONS

4.1 SUMMARY

Controlling electrode composition and porosity in a SOFC is very challenging; however, the 3D direct write process provides a novel approach to engineering these structures. A graded electrode structure, which is desirable from a mass transport perspective, has been fabricated using nScrypt's 3D direct write microextrusion method. 3D direct write microextrusion allows precise local control of material and/or structure and can be used to produce engineered porous electrodes. This also translates into ease of quantifying/modeling the structure as the dimensions are known before printing or can be easily measured under a light microscope.

The change in degree of porosity of electrode by varying the graphite loading fraction has been experimentally mapped out qualitatively. The feasibility of changing the composition/porosity within a layer has been demonstrated, which opens up possibilities of varying the physical structure within a layer as well as between layers.

The baseline has been set to create a BSC like freeze tape cast structure. The engineered structure has tortuosity close to one (i.e. straight line path) which improves gas flow through the porous membrane. Low tortuosity in the ribs also reduces conductive path length and associated resistivity losses. The surface area of the electrodes can be increased by fabricating closely spaced ribs having scalloped vertical wall surfaces which have higher surface area than vertical walls. Increase in surface area positively impacts the ionic and electrical properties of electrodes and hence the cell.

An electrolyte-supported button cell fabricated via this technique showed OCV ~ 1 V @ 800 °C which is comparable with button cells fabricated using other technologies. Porous anode, porous cathode and dense electrolyte can all be fabricated using 3D direct write methods.

Last, this method is capable of fabricating multifunctional, multimaterial components with complex geometries; one simple example is the concentric spiral structure. These structures provide enhanced mechanical strength in all directions and balanced shrinkage stresses. This eliminates the propensity of freeze tape cast structures to shrink primarily along one axis.

4.2 FUTURE WORK

4.2.1 Next Steps

The next logical step in this research is to fabricate a number of SOFC button cells from a variety of materials and to begin comparing the performance of spiral or concentric ring architectures with those of conventionally porous electrodes.

The work presented here demonstrates the feasibility with production of structured electrodes via direct-write techniques and further engineering it by adjusting the process parameters. Various geometries are possible using 3D direct write methods, but the longer term question still remains “what should the structure look like”? As our understanding of the science improves and models are developed, they can be used to suggest specifically what the structure we print should look like. The next step would then be to use the direct-write techniques described in this thesis to experimentally validate scientific models.

nScrypt’s pneumatically actuated multi-material micro-mixing tool is potentially a very useful method for grading chemical composition on the fly. It can grade the material composition between electrolyte and electrode as well as for grading the pore former concentration in the ink being extruded (i.e. create graded porosity). This method is well suited for extruding “mixed” low vicious inks, but faces challenges when it comes to mixing highly viscous inks and then co-extruding them. Thus, the future work should investigate positive displacement multi-material dispensing for this purpose

4.2.2 Co-Extrusion

As stated before, co-extrusion enables one to print finer lines and channels. If a line width of *x* is possible under certain conditions, then co-extruding electrode and graphite pastes at a ratio of 7:3 will theoretically allow one to produce rib widths of 0.7*x* and channel widths of 0.3*x*. Co-extrusion can be applied to co-extrude 3 inks and potentially more.

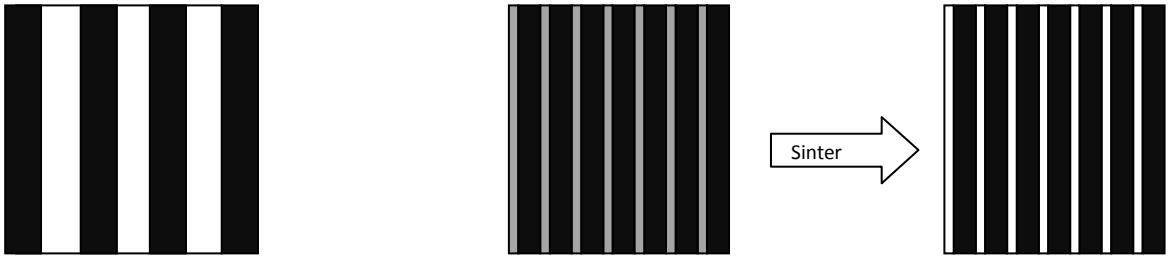

a) 3D Printing (Lines and Spaces) **b) Co-extrusion with 3D Printing, Pre (left) and Post (Right) Sintered**

Figure 44 Co-extrusion Process

By way of example, assume that a total of 4 lines and 3 spaces of equal width are printed as shown in Figure 44(a). If two inks are co-extruded under the same conditions as the lines were originally printed, then 7 co-extruded lines can be printed side-by-side (Figure 44(b)). When sintered, the fugitive material burns off leaving behind a channel. The resulting profile when compare to 3D printed process can be seen in Figure 44(b). In the area where there were 4 lines and 3 spaces, there are now 7 lines and 7 spaces that are narrower in width. This drastically increases the surface area of the electrodes. The ratio between the lines and spaces can be controlled via process characterization.

The image below shows results from a preliminary attempt at co-extrusion of a fuel cell ink and graphite ink (Figure 45). The lines were printed side-by-side, ensuring that there were maximum contact and minimum overlap in-between lines. Obtaining consistent flow rates between co-extruded inks with very different rheological properties is a challenge; however the process is conceptually quite simple and warrants further exploration. The graphite ink and

NiO-YSZ paste were co-extruded with no gaps in-between lines. After sintering, the graphite portion burned off leaving behind a long channel [Figure 45(b)]. The resulting profile consisted of a rib and channel (similar to BSC like structure). This process can be further developed to create finer lines and channels as the ratio of line to channel width can be controlled via process parameters.

a) Pre-sintered profile **b) Post sintered profile**

Figure 45 Co-extrusion results

4.2.3 Alternate 3D Direct Write Tool – Optomec

Optomec's Aerosol Jet process (http://www.optomec.com) begins with an atomizer that aerosolizes a source ink. The aerosol stream is carried to a ceramic nozzle in flowing nitrogen carrier gas. Particles in the resulting aerosol stream out through a nozzle that is directed at the substrate, thereby resulting in deposition. Patterning is accomplished by movement of a computer-controlled platen, and the relatively large (>5mm) standoff distance from the deposition head to the substrate allows accurate material deposition on non-planar substrates, over existing structures and into channels.

4.3 CONCLUSIONs

This thesis has demonstrated that 3D direct write printing is a promising approach to locally controlling the porosity, composition, and structure of SOFC components. Its unique ability to vary porosity/composition within a layer opens up possibilities of varying composition within a layer/plane (most research in the past has been in varying composition in–between layers). Although future work will be needed to fully exploit the potential advantages of this approach, it has great possibilities for:

- Enhancing mass transport through the porous layers
- Shortening conductive path lengths and reducing ohmic losses
- Overcoming durability issues associated with mismatches in coefficient of thermal expansion between dissimilar materials
- Facilitating solution infiltration of cathode layers

REFERENCES

[1] Ishizaki, Kozo, Sridhar Komarneni and Makoto Nanko (1998). *Porous Materials (Materials Technology Series).* New York: Springer.

[2] Vassilis Karageorgiou, D. K. (2005). Porosity of 3D biomaterial scaffolds and osteogenesis. *Biomaterials, 26* (27), 5474-5491.

[3] N.P Brandon and D.J Brett (2006). Engineering porous materials for fuel cell applications. *Phil. Trans. R. Soc. A,* 364, 147-159.

[4] Jung-Hoon Song, Nigel M. Sammes, Sun-Il Park, Seongjae Boo, Ho-Sung Kim, Hwan Moon, Sang-Hoon Hyun (2008). Fabrication and Characterization of Anode-Supported Planar Solid Oxide Fuel Cell Manufactured by a Tape Casting Process. *Journal of Fuel Cell Science and Technology*, 5 (2), .

[5] Holtappels, P., Sorof, C., Verbraeken, M. C., Rambert, S. and Vogt, U. (2006). Preparation of Porosity–Graded SOFC Anode Substrates. *Fuel Cells*. 6(2), 113-116.

[6] K. Kendall and S.C. Singhal. (2004). *High-temperature Solid Oxide Fuel Cells Fundamentals, Design and Applications*. St. Louis: Elsevier Science.

[7] *FCT Fuel Cells: Types of Fuel Cells*. (n.d.). Retrieved September 10, 2010, from http://www1.eere.energy.gov/hydrogenandfuelcells/fuelcells/fc_types.html

[8] *NScrypt Inc. - Precise, Conformal, Reconfigurable Dispensing Technologies*. (n.d.). Retrieved from http://www.nscryptinc.com

[9] R.M. Ormerod (2003). Solid Oxide Fuel Cells. *Chemical Society Reviews*, 32, 17-29.

[10] *EERE: Hydrogen and Fuel Cells*. (n.d.). Retrieved September 10, 2010 from http://www.eere.energy.gov/topics/hydrogen_fuel_cells.html

[11] De Guire, E. J. (n.d.). *Solid Oxide Fuel Cell*. Retrieved from http://www.csa.com/discoveryguides/fuecel/overview.php

[12] *Fuel Cells Overview*. (n.d.). Retrieved from http://www.fchea.org

[13] *Ceramic Fuel Cells Limited:: Applications*. (n.d.). Retrieved March 14, 2010, from http://www.cfcl.com.au/Applications/

[14] *Fuel Cell Basics: Benefits*. (n.d.). Retrieved from http://www.fuelcells.org/basics/benefits.html.

[15] *Benefits of Fuel Cell Technology*. (n.d.). Retrieved from http://www.fuelcellenergy.com

[16] Singhal, S. C. (n.d.). *Solid Oxide Fuel Cells*. Retrieved from http://www.electrochem.org

[17] Ellen Ivers-Tiffee, Andre Weber, Dirk Herbstritt (2001). Materials and technologies for SOFC-components. *Journal of the European Ceramic Society*. 21 (10-11), 1805-1811.

[18] P. E. Gannon, A. Kayani, C. V. Ramana, M. C. Deibert, R. J. Smith, and V. I. Gorokhovsky, Electrochem (2008). Simulated SOFC Interconnect Performance of Crofer 22 APU with and without Filtered Arc CrAlON Coatings. *Electrochemical and Solid-State Letter,* 11(4), B54-B58.

[19] Fergus, Jeffrey W. (2009). *Solid Oxide Fuel Cells: Materials Properties and Performance*. Boca Raton: CRC Press.

[20] N.M. Sammes, Y. Du, R. Bove (2005). Design and fabrication of a 100 W anode supported micro-tubular SOFC stack. *Journal of Power Source,* 145 (2), 428-434.

[21] Hae-Gu Park, Hwan Moon, Sung-Chul Park, Jong-Jin Lee, Daeil Yoon, Sang-Hoon Hyun, Do-Heyoung Kim (2010). Performance improvement of anode-supported electrolytes for planar solid oxide fuel cells via a tape-casting/lamination/co-firing technique. *Journal of Power Source,* 195 (9), 2463-2469.

[22] NASA Tech Brief (2007). *Fabrication of Functionally Graded and Aligned Pores Via Tape Cast Processing*. LEW-17628-1.

[23] Glenn Research Center. *Freeze Tape Casting of Functionally Graded Porous Ceramic* (n.d.). Retrived from http://www.nasa.gov

[24] Stephen W. Sofie (2007) "Fabrication of Functionally Graded and Aligned Porosity in Thin Ceramic Substrates with the Novel Freeze-Tape-Casting Process. *Journal of the American Ceramic Society*, 90 (7), 2024–2031.

[25] Masayuki NAKATA, Kimiaki Tanihata, Shunro Yamaguchi and Katsuaki Suganuma (2005). Fabrication of Porous Alumina Sintered Bodies by a Gelate-Freezing Method. *J. Ceram. Soc. Japan*, 113, 712-715.

[26] F. Dogan and S.W. Sofie (2002). Microstructural Control of Complex-Shaped Ceramics Processed by Freeze Casting. *Ceram.Forum Int./Ber.DKG*, 79 (5), E35-E38.

[27] Thomas L. Cable, Stephen W. Sofie (2007). A symmetrical, planar SOFC design for NASA's high specific power density requirements. *Journal of Power Sources*, 174 (1), 221-227.

[28] Dr. Nguyen Minh, Kurt Montgomery. *Tape Calendering Manufacturing Process for Multilayer Thin-Film Solid Oxide Fuel Cells*. Retrieved from http://www.osti.gov

[29] Min-Fang Han, Hui-Yan Yin, Wen-Ting Miao, Su Zhou (2008). Fabrication and properties of anode-supported solid oxide fuel cell. *Solid State Ionics*, 179 (27-32), 1545-1548.

[30] D. Rotureau, J.-P. Viricelle, C. Pijolat, N. Caillol, M. Pijolat. Development of a planar SOFC device using screen-printing technology. *Journal of the European Ceramic Society*, 25 (12), 2633-2636.

[31] Flesner, R. (2009). *Modeling of Solid Oxide Fuel Cell functionally graded electrodes and a feasibility study of fabrication techniques for functionally graded electrodes.* (Master's Thesis), Retrieved from ProQuest Dissertations and Theses. (Accession Order No AAI1473204)

[32] J. Ding, J. Liu (2008). An anode-supported solid oxide fuel cell with spray-coated yttria-stabilized zirconia (YSZ) electrolyte film. *Solid State Ionics*, 179, 1246–1249.

[33] Wang Z., Weng W., Chen K., Shen G., Du P., Han G (2008). Preparation and performance of nanostructured porous thin cathode for low-temperature solid oxide fuel cells by spin-coating method. *Journal of Power Sources*, 175 (1), 430-435.

[34] Bhavana Godbole, Nitu Badera, S.B. Shrivastav and V. Ganesan (2009). A simple chemical spray pyrolysis apparatus for thin film preparation. *Jl. of Instrum. Soc. of India*, 39 (1), 42-45.

[35] Seiichi Suda, Mikio Itagaki, Eri Node, Seiji Takahashi, Mitsunobu Kawano, Hiroyuki Yoshida, Toru Inagaki. Preparation of SOFC anode composites by spray pyrolysis. *Journal of the European Ceramic Society*, 26 (4-5), 593-597.

[36] L.R. Pederson, P. Singh, X.-D. Zhou (2006). Application of vacuum deposition methods to solid oxide fuel cells. *The World Energy Crisis: Some Vacuum-based Solutions*, 80 (10), 1066-1083.

[37] Nai-Tao Yang, Xiaoyao Tan, Xiu-Xia Meng, Yimei Yin, and Zi-Feng Ma (2009). Fabrication of Anode Supported Micro Tubular SOFCS by Dip-Coating Process on NiO/YSZ Hollow Fibers. *ECS Trans.*, 25, 881.

[38] Yonglian Zhang, Jianfeng Gao, Dingkun Peng, Meng Guangyao, Xingqin Liu, (2004). Dip-coating thin yttria-stabilized zirconia films for solid oxide fuel cell applications. *Ceramics International*, 30 (6), 1049-1053.

[39] *TWI - Manufacturing, Engineering, Materials and Joining Specialists, Plasma Spraying*. (n.d.). Retrieved from http://www.twi.co.uk/content/surf23.html

[40] T. Franco, Z. HoshiarDin, P. Szabo, M. Lang, and G. Schiller (2007). Plasma Sprayed Diffusion Barrier Layers Based on Doped Perovskite-Type LaCrO[sub 3] at Substrate-Anode Interface in Solid Oxide Fuel Cells. *Journal of Fuel Cell Science and Technology*, 4, 406.

[41] Rob Hui, Zhenwei Wang, Olivera Kesler, Lars Rose, Jasna Jankovic, Sing Yick, Radenka Maric, Dave Ghosh (2007). Thermal plasma spraying for SOFCs: Applications, potential advantages, and challenges. *Journal of Power Sources*, 170 (2), 308-323.

[42] B. Li, K.H. Church, P.A. Clark (2007). Robust Direct-Write Dispensing Tool and Solutions for Micro/Meso-Scale Manufacturing and Packaging. *ASME Conf. Proc.*, 2007, 715-721.

[43] Melanie Kuhn, Teko Napporn, Michel Meunier, Srikar Vengallatore and Daniel Therriault. Direct-write microfabrication of single-chamber micro solid oxide fuel cells. *Journal of Micromechanics and Microengineering*, 18 (1), 015005.

[44] Kuhn, M. (2009). *Direct-write microfabrication and characterization of single-chamber micro solid oxide fuel cells with coplanar electrodes*. VDM Verlag Dr. Müller.

[45] D. Young, A.M. Sukeshini, R. Cummins, H. Xiao, M. Rottmayer, T. Reitz (2008). Ink-jet printing of electrolyte and anode functional layer for solid oxide fuel cells. *Journal of Power Sources*, 184 (1), 191-196.

[46] Silas Towne, Vish Viswanathan, James Holbery, Peter Rieke (2007). Fabrication of polymer electrolyte membrane fuel cell MEAs utilizing inkjet print technology. *Journal of Power Sources*, 171 (2), 575-584.

[47] M. Sukeshini, R. Cummins, T. L. Reitz, and R. M. Miller (2009). Inkjet Printing of Anode Supported SOFC: Comparison of Slurry Pasted Cathode and Printed Cathode. *Electrochem. Solid-State Lett.*, 12, B176.

[48] *DOE Office of Fossil Energy*. (n.d.). Retrieved from Fuel Cell Handbook: http://www.fossil.energy.gov/programs/powersystems/fuelcells/publications

[49] *DOE - National Energy Technology Laboratory (n.d.).* Retrieved from NETL: Solid State Energy Conversion Alliance (SECA) - Industry Teams: http://www.netl.doe.gov/technologies/coalpower/fuelcells/seca/industry.html

[50] *DOE - National Energy Technology Laboratory (n.d.).* Retrieved from NETL: Solid State Energy Conversion Alliance (SECA) - Reference Shelf: http://www.netl.doe.gov/technologies/coalpower/fuelcells/seca/refshelf.html

[51] Hengyong Tu and Ulrich Stimming (2004). Advances, aging mechanisms and lifetime in solid-oxide fuel cells. *Journal of Power Sources*, 127 (1-2), 284-293.

[52] S. C. Singhal (2000). Advances in solid oxide fuel cell technology. *Solid State Ionics*, 135 (1-4), 305-313.

[53] Rudolf Henne (2007). Solid Oxide Fuel Cells: A Challenge for Plasma Deposition Processes. *Journal of Thermal Spray Technology*, 16 (3), 381-403.

[54] R. Henne, M. Lang, M. Müller, R. Ruckdäschel, G. Schiller (1999). Manufacturing Solid Oxide Fuel Cells – A Challenge for DC and RF Plasma Deposition Processes. *Annals of the New York Academy of Sciences*, 891, 124-136.

[55] Detlev Stover, Dag Hathiramani, Robert Vassen, Rajiv J. Damani (2006). Plasma sprayed components for SOFC applications, Surface and Coatings Technology. *The 2nd International Meeting on Thermal Spraying - 2nd RIPT*, 201 (5), 2002-2005.

[56] Xu, X., Xia, C., Xiao, G., and Peng, D. (2005). Fabrication and Performance of Functionally Graded Cathodes for It-Sofcs Based on Doped Ceria Electrolytes. *Solid State Ionics*, 176(17-18), 1513-1520.

[57] Hart, N. T., Brandon, N. P., Day, M. J., and Lapena-Rey, N. (2002). Functionally Graded Composite Cathodes for Solid Oxide Fuel Cells. *Journal of Power Sources*, 106(1-2), 42-50.

[58] Ni, M., Leung, M. K. H., and Leung, D. Y. C. (2007). Micro-Scale Modeling of Solid Oxide Fuel Cells with Micro-Structurally Graded Electrodes. *Journal of Power Sources*, 168(2), 369-378.

[59] Ni, M., Leung, M. K. H., and Leung, D. Y. C. (2007). Micro-Scale Modeling of a Functionally Graded Ni-YSZ Anode. *Chemical Engineering and Technology*, 30(5), 587-592.

[60] NASA Glenn Ceramics Branch. *Solid Oxide Fuels Cells and Electrolysis Membrane* (n.d). Retrived from: http://www.grc.nasa.gov/WWW/StructuresMaterials/Ceramics/research_solid.html

Appendix A

A sample script to fill a 6mm circle with 600 µm step-over lines on a nScrypt tool

absolute

```
pen  SMARTPUMP_1
speed    30
trigvalverel        1.2       2
move    -6          0         0
move    -5.99       -0.34     0
move    -5.99       0.34      0
move    -5.39       2.63      0
move    -5.39       -2.63     0
move    -4.79       -3.6      0
move    -4.79       3.6       0
move    -4.19       4.28      0
move    -4.19       -4.28     0
move    -3.59       -4.8      0
move    -3.59       4.8       0
move    -2.99       5.19      0
move    -2.99       -5.19     0
move    -2.39       -5.49     0
move    -2.39       5.49      0
move    -1.79       5.72      0
move    -1.79       -5.72     0
move    -1.19       -5.87     0
move    -1.19       5.87      0
move    -0.59       5.96      0
move    -0.59       -5.96     0
move    0.01        -5.99     0
move    0.01        5.99      0
move    0.61        5.96      0
move    0.61        -5.96     0
move    1.21        -5.87     0
move    1.21        5.87      0
move    1.81        5.71      0
move    1.81        -5.71     0
move    2.41        -5.48     0
move    2.41        5.48      0
move    3.01        5.18      0
move    3.01        -5.18     0
move    3.61        -4.78     0
move    3.61        4.78      0
move    4.21        4.27      0
move    4.21        -4.27     0
move    4.81        -3.58     0
move    4.81        3.58      0
move    5.41        2.58      0
move    5.41        -2.58     0
valverel    0       10
move 14   0   0
```